LENS
Universitá degli studi di Firenze

Characterization of Charge Transfer Processes in Bipyridine Dyes by Transient Absorption and Time Resolved Infrared Spectroscopies

Sandra Mosquera Vázquez

Dottorato in Scienze Chimiche
Ciclo XXIII

Supervisor : Prof. Roberto Righini

Contents

1 Introduction

1.1 Electron Transfer

Photoinduced electron transfer is the pivotal process in photosynthesis, photoimaging, photo-reaction mechanisms and optoelectronic devices. Studying this process in well-defined artificial systems may lead to further insight into the primary events occurring in the biological processes responsible for a large part of the energy production on earth. Not only is the energy in all 'food and feed' on earth derived from the light induced conversion of carbon dioxide and water into carbohydrates, but also all the energy in fossil fuels like oil, natural gas and coal. They were initially fixed by phototrophic organisms. Light induced electron transfer is a process in which an electron is transferred from an electron donating species (D) to an electron accepting species (A). Prior to electron transfer one of the components is excited with light:

$$D + A \xrightarrow{h\nu} D^* + A \tag{1.1}$$

$$D^* + A \xrightarrow[\text{E.T.}]{} D^{+\bullet} + A^{-\bullet} \tag{1.2}$$

by this simple sequence, light energy is converted into electrochemical energy. Subsequent to the electron transfer a charge transfer state is created, which is a dipolar species, consisting of the radical cation of the donor and the radical anion of the acceptor.

The charge transfer state created can undergo many different process. For example, In the photosynthetic reaction (after the energy transfer from the light harvesting system to the special pair) a first electron transfer from the special pair to the pheophytin P(in 3 ps) is followed by a second electron transfer from the P^- to the ubiquinone Q_A (200 ps). Next, the electron is transferred from Q_A to a second quinone Q_B (in 100 μs).

Thus, the first electron transfer is followed by two consecutive steps. In the final state chemistry takes over: Q_B takes up two protons (after two electron transfer cycles) and leaves its site, traverses the membrane in which the system is embedded and releases its protons again. Thus a proton coupled electron transfer process is accomplished, by which light-energy is converted into an electrochemical proton gradient, by which the biological synthesis of energy rich molecules like ATP (adenosine triphosphate) is driven.

Another process that can follow charge separation (or forward electron transfer) is simply charge recombination (or back electron transfer) leading to the initial state. This is in fact a very common process, which is often the fate of a charge transfer state.

This charge recombination can occur by a dark (non-radiative) process, but there exist many systems in which the charge transfer state undergoes a radiative charge recombination. The wavelength of the emission of this process (often called charge transfer fluorescence or, more accurately, charge recombination fluorescence) is very dependent on the environment of the dipolar charge transfer state. A polar environment stabilizes this state and thus lowers its energy and thereby shifts the emission to the red. These types of systems can be used as a polarity (and mobility) probe.

1.1.1 Historical Background

The understanding of organic charge transfer complexes[1] started in the late 1940's, early 1950's with the reports of Benesi and Hildebrand (1949), who observed new absorption bands in solutions of aromatic hydrocarbons and iodine and the idea of partial charge transfer in the ground-state of Brackman.

The Mulliken model (1952) for electron- donor acceptor complexes, and the discovery of excimer formation by Förster and Kaspar in 1954 were essential steps that have led to the extensive developments in the field of electron- donor acceptor systems in the last decades.

Early examples of a donor and acceptor that are covalently linked were reported in 1969.[2] Linking donor and acceptor to each other by covalent bonding has proved to be an important step towards a better understanding of the electron transfer process. A large number of studies on photoinduced intramolecular electron transfer in covalently linked donor-bridge-acceptor compounds incorporating a hydrocarbon bridge to link two chromophores,

have been published during the past decades. Thus, a lot of information concerning distance dependence, symmetry effects, influence of the bridge configuration and the energetic dependence of CT processes has been obtained[3,4] The predictions made in the R.A. Marcus (Nobel Price winner) were first confirmed by this type of donor-bridge-acceptor systems. These studies have also shown that photoinduced intramolecular charge separation can be accomplished in systems in which donor and acceptor are spaced up to 15 Å by a saturated hydrocarbon bridge. This bridge not only establishes exact inter chromophore distance, it is also strongly involved in the electronic coupling between donor and acceptor, that is required for photoinduced electron transfer. Mixing of the σ and σ^* orbitals of the bridge with the donor and acceptor π orbitals, results in a mixing of the electronic wave functions of the latter two, resulting in electronic coupling.

1.1.2 Theory

A photoinduced electron transfer from D to A results in the formation of a charge separated state which consists of the corresponding radical cation and anion, and the process is in direct competition with the radiative and nonradiative processes that are present in the excited state of A (or D). Therefore electron transfer can be regarded as an extra deactivation path of the locally excited (singlet) state that can exist next to internal conversion (IC), inter system crossing (ISC) to the triplet manifold (both iso-energetic) and emission (F).

Thus the occurrence of electron transfer should diminish both the emission quantum yield and excited state lifetime. There are, however, other mechanisms that can be responsible for fluorescence quenching: e.g. energy transfer, proton transfer, hydrogen bonding and the external heavy atom effect. Only by careful examination of the experimental conditions, and chosen variations thereof, we can establish the cause of fluorescence quenching. Energy transfer can only proceed from a state of a certain multiplicity to a state with a lower energy with the same multiplicity. Thus, from the absorption and emission characteristics it can be predicted whether energy transfer is possible. Proton transfer can be a highly efficient and fast nonradiative decay channel, i.e. an intramolecular vibrational relaxation. The presence of hydrogen bonds can also introduce a non-radiative deactivation path, i.e. many compounds do not fluoresce in protic solvents. The heavy atom effect enhances spin orbit coupling, by which the rate of inter system crossing is increased and thus the lifetime of the excited singlet state is reduced. Electron transfer depends on the redox properties of the donor acceptor couple together with the excitation energy. In polar solvents it can be said that the Gibbs free energy change for charge separation (ΔG_{CS}), is

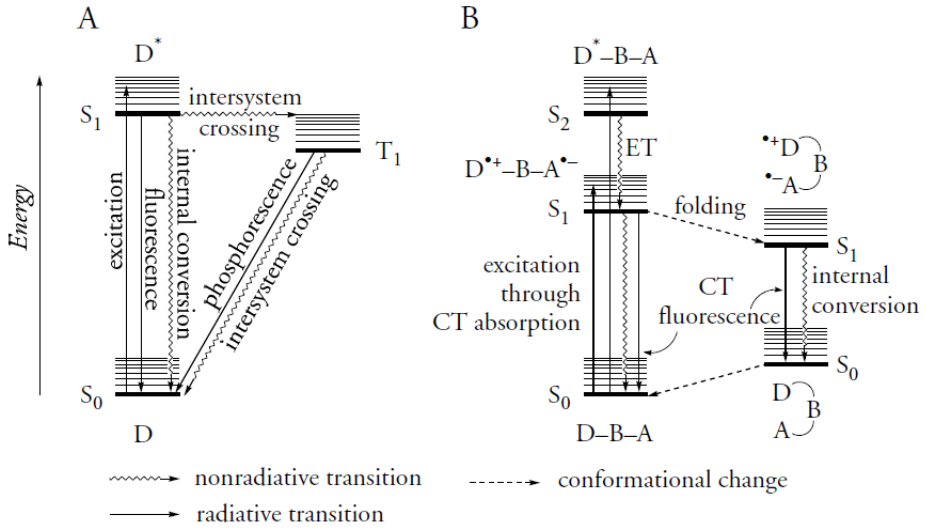

Figure 1.1: Schematic diagram depicting the relative energies of the most relevant spectroscopic states of A a monochromophoric molecule D and (B) a bichromophoric molecule D-A. note that in (B) many others states with the accompanying transition may play a role in deactivating the D*-B-A state (including those depicted in (A)). Although ET is marked as a nonradiative transition, it has been shown that electromagnetic radiation is emitted during intramolecular ET transitions.

given by

$$\Delta G_{CS} = e^{E^0(D^+/D) - E^0(A^-/A)} - \Delta E_{0,0} \tag{1.3}$$

(the 'polar driving force'). In other words, the energy put into the system by excitation ($-\Delta E_{0,0}$) should be more than the energy it costs to oxidize the donor and to reduce the acceptor. The fluorescence quantum yield (Φ_{ref}) and the fluorescence life time (τ_{ref}) of a certain (reference) species can be described, using the rates (κ) of the processes (F, IC and ISC see figure 1.1) by:

$$\Phi_{ref} = \frac{\kappa_f}{\kappa_f + \kappa_{ic} + \kappa_{isc}} \tag{1.4}$$

$$\tau_{ref} = \frac{\kappa_f}{\kappa_f + \kappa_{ic} + \kappa_{isc}} \tag{1.5}$$

The introduction of a second chromophore (or electroactive) group in the molecule that is separated from the first one by a bridge may lead to a number of other decay processes. Which processes proceed fastest and dom-

inate the decay depends on, for instance, the nature of the chromophores, the chromophore-chromophore orientation and both the length and nature of the intervening bridge.

The D-B-A compounds considered in this thesis can have in addition to the locally excited states of the donor and acceptor at least two extra states of low energy: a charges-separated S_1 state and a charge-separated T_1 state. Only the S_1 state is depicted in Figure 1.1. The internal conversion process from the S_2 to the S_1 state is the ET process. When the charge-separated state is formed out of a locally excited acceptor state it is better to speak of hole transfer (HT):

$$D-A \xrightarrow{h\nu} D^*-A \xrightarrow{ET} D^{\cdot+}-A^{\cdot-}$$

$$D-A \xrightarrow{h\nu} D-A^* \xrightarrow{HT} D^{\cdot+}-A^{\cdot-}$$

In case of a strong electronic coupling between the ground state, the charge-separated (CS) state and a locally excited state or between the ground state and a CS state, a charge transfer (CT) absorption band may be discernible, which represents direct excitation to the CS state. The energy level of a CS state depends strongly on the solvent polarity. Due to the very polar nature of this state, it is more stabilized in polar than in non-polar solvents.

When a flexible bridge is used, the attractive coulomb force between the opposite charges in a CS state can induce conformational changes in the molecule that will bring donor and acceptor closer together. This is indicated as 'folding' in Figure 1.1. Note that the ground state produced by fluorescence from such a folded CS state is higher in energy than an unfolded ground state.

The efficiency of the ET step depends on the rate constant κ_{ET} of the ET step itself and the rate constants of the competing processes depopulating D^*-A. In studies on ET processes the rate constants are determined mainly by the following techniques: time-resolved absorption spectroscopy, time-resolved fluorescence spectroscopy and time-resolved microwave conductivity. This gives a lifetime τ which in the case of an excited donor molecule D^* (or acceptor A^*) is related to the sum of the rates of all decay processes

$$\tau(D^*) = \frac{1}{\sum \kappa_{decay}} = \frac{1}{\kappa_r + \kappa_{nr}} \tag{1.6}$$

The decay processes are divided in radiative (κ_r) and non-radiative (κ_{nr}) decay processes. The quantum yield of fluorescence Φ_r is defined as the fraction of excited molecules that decay via fluorescence. When both Φ_r

and $\tau(D^*)$ are known, (κ_r can be calculated via

$$\tau(D^*) = \frac{\Phi_r}{\kappa_r} \tag{1.7}$$

When ET with a rate κ_{ET} contributes to the decay of the excited state of the donor expression 1.7 becomes

$$\tau(D^* - A) = \frac{1}{\kappa_r + \kappa_{nr} + \kappa_{ET}} \tag{1.8}$$

When it is assumed that the introduction of an acceptor does not influence the rates of other processes deactivating the excited donor, κ_{ET} can be obtained from

$$\kappa_{ET} = \frac{1}{\tau(D^* - A)} - \frac{1}{\tau(D^*)} \tag{1.9}$$

$$\kappa_{ET} = \frac{\Phi_r(D^*)}{\Phi(D^* - A)\tau^(D^*)} - \frac{1}{\tau_r(D^*)}[10pt] \tag{1.10}$$

A more direct way to determine κ_{ET} is to measure the rise time of an absorption typical for the CS state $D^{\cdot+}$-$A^{\cdot-}$. Unfortunately, this is not always possible.

1.1.3 Marcus and Weller

For ET, several theories at different levels of sophistication have been developed. Here we present a brief summary of the most elementary theory of ET, which is useful for the explanation of many experimental results. This theory was mainly developed by Rudolph Marcus in a series of articles published in 1950's and 1960's.

In classical ET theory, a collection of reactant molecules r in solution undergoes electron transfer to form a product p. In the case of photoinduced ET, $r = D^* - A$) and p = $D^{\cdot+}$-$A^{\cdot-}$. It is assumed that the initial and final states are weakly coupled (the exact meaning of which is defined in the next pages, but π-conjugated systems are not taken into account). The state energies of r and p depend, in general, on all the nuclear coordinates of the system: those of r and p, respectively, and those of the solvent molecules surrounding them. These coordinate-dependent energies constitute the multidimensional potential energy surfaces of the two states within the Born-Oppenheimer approximation. In ET theory the many nuclear coordinates of the system are collected in a single reaction coordinate q. Moreover, the Gibbs free

energies G instead of the potential energies of the r and p states are usually considered, since the former can be well represented as quadratic functions of q. In the free energy representation, q may be defined as the difference between (nuclear) orientation polarization and vibrational energy of the r and p states ($q = G_r - G_p$). The parabolas that represent r and p states are depicted in Figure **??**. Note that in classical ET theory the curvature of the parabolas representing the r and p states is assumed to be the same.

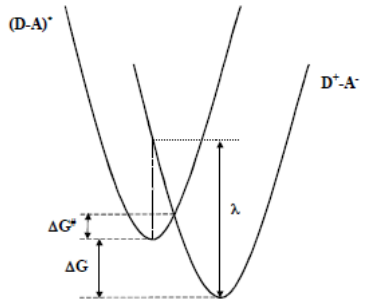

Figure 1.2: State free energy G versus reaction coordinate q for an exergonic electron transfer reaction r $\longrightarrow$ p. Indicated are the change of Gibbs free energy ΔG^0, the free energy barrier $\Delta G^{\ddagger}$,and the reorganization energy λ associated with the reaction.

The ET process starts with a distortion of the reactant state r along the reaction coordinate from its equilibrium position A to position B, the transition state. The cost of this process is the activation energy $\Delta G^{\ddagger}$. The reactant enters the product state and finally relaxes to its equilibrium geometry C. The change in free energy associated with the reaction (or transition) is ΔG^o. Formally, another trajectory is possible in which firstly the reactant state is distorted to the equilibrium geometry of the product state C, without transfer of an electron, and secondly ET occurs, which corresponds to a vertical displacement from the reactant curve to the minimum of the product curve. The first step includes solvent reorientation to respond to the charges in the product state (which are not yet present) and the molecular deformation of the reactant into the equilibrium geometry of the product. Electronic polarization is not included. The change in free energy associated with this step is called the reorganization energy λ. The reorganization energy can be divided in a term arising from the nuclear deformation of the reactant itself, the intramolecular reorganization energy λ_i, and a term due to the solvent reorientation, λ_s.

In the classical treatment of ET an equation for the solvent reorganization energy was derived based upon a model in which donor and acceptor are represented as spheres and are immersed in a solvent bath characterized by a dielectric constant ε and refractive index n. Since the molecules of the

solvent are not treated explicitly, such a model is called a solvent continuum model. The radii of the spheres are given by r_D and r_A. The spheres are separated by a centre-to-centre distance R_{DA}. The solvent reorganization energy in this model is given by

$$\lambda_s = \frac{e^2}{4\pi\varepsilon_0}\left(\frac{1}{2r_D}+\frac{1}{2r_A}+\frac{1}{r_{DA}}\right)\left(\frac{1}{n^2}-\frac{1}{\varepsilon_o}\right) \tag{1.11}$$

It appears that irrespective of whether donor and acceptor are represented by spheres or ellipsoids, it is usually possible to approximate λ_s as:

$$\lambda_s \cong B\left(\frac{1}{n^2}-\frac{1}{\varepsilon_o}\right) \tag{1.12}$$

with B a solvent independent parameter whose value depends on the model and molecular dimensions chosen.

A CS state is stabilized in polar solvents (i.e. solvents with a high dielectric constant and/or a large value of the square of the refractive index, n^2, which are measures for the low and high frequency polarizability of the solvent, respectively). This stabilization is due to a considerable reorientation of the solvent dipole moments which is taken into account in λ_s.

According to Marcus theory the barrier for ET is given by

$$\Delta G^{\ddagger} = \frac{\left(\lambda_s + \Delta G^0\right)^2}{4\lambda_s} \tag{1.13}$$

From the standard Arrhenius relationship between activation free energy, temperature and rate constant, the rate for ET is given by

$$\kappa_{ET} = Ae^{\left(\frac{-\Delta G^{\ddagger}}{\kappa_B T}\right)} = Ae^{\left(\frac{(-\lambda+\Delta G^0)^2}{4\lambda\kappa_B T}\right)} \tag{1.14}$$

Here A is a prefactor which depends on the crossing of the frequency the barrier top, κ_B is the Boltzmann constant and T the temperature. The frequency A can be expressed as the product of a nuclear frequency ν_n and an electronic transmission coefficient, κ_e which in classical theory is taken to be unity so that every crossing of the barrier leads to ET

$$A = \nu_n \kappa_e \tag{1.15}$$

The nuclear frequency is related to molecular vibrations of the reactant.

Molecular vibrations typically have a frequency in the order of 10^{13} s_1 and therefore, classical ET theory predicts a maximum ET rate of $\sim 10^{13}$ s_1.

1.1.4 'Normal' and 'Inverted' Regimes

The Marcus theory implies that barrierless electron transfer can occur if $\lambda = -\Delta G_{CS}$. This is called the optimal region. $\lambda > -\Delta G_{CS}$ the electron transfer rate increases with larger driving forces. However, in the so-called Marcus inverted region, if $\lambda < -\Delta G_{CS}$, the rate decreases with larger driving forces. This is counter-intuitive. The barrier is very thin in the inverted region. This facilitates nuclear tunneling and thus, in processes in the inverted region (charge recombination is often an inverted region process) the observed rates are higher than expected from the classical Marcus theory. Typical (classical) free energy diagrams associated with these regimes are given in Figure 1.3

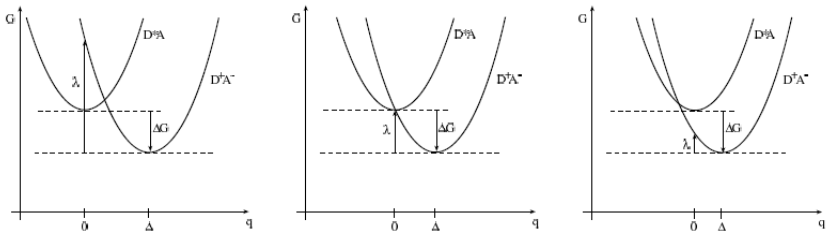

Figure 1.3: The different regions in the Marcus theory of electron transfer , together with the representations of the Gibbs free energy change , and the reorganization energy.

1.1.5 The electronic coupling

According to what reported in the previuos paragraph, the ET is induced by coupling between the two states with an exchange interaction $V_{av,b\omega}$

$$V_{av,b\omega} = \int\int \Psi_a^*(r,q) X_{av}^*(q) \widehat{V} \Psi_b^*(q) X_{b\omega}^*(q) dq dr \qquad (1.16)$$

$\widehat{V}$ couples every vibronic substate of the initial state $|av\rangle$ with an energy E_{av} to a multiplicity of vibronic charge separated states $\{|b\omega\rangle\}$ and energies $E_{b\omega}$, which are quasi-degenerate with the initial state.

The electronic transition takes place instantly without change of nuclear coordinates (Born-Oppenheimer approximation); the electronic wave function depends only weakly on the nuclear coordinates (Franck-Condon

principle). The double integral in equation 1.16 can then be separated:

$$V_{av,b\omega} = \langle av|\widehat{V}|b\omega\rangle = \tag{1.17}$$
$$= \langle \Psi_{a,v}(r,q)|\widehat{V}|\Psi^*_{b,\omega}(q,r)\rangle\langle X_{av}|X_{b,\omega}\rangle \approx$$
$$\approx V\langle X_{av}|X_{b,\omega}\rangle$$

For ET reactions, only the overlap of nuclear wavefunctions and electronic coupling is relevant. Depending on the magnitude of the electronic coupling V two limiting cases can be separated:

- For large V , the potential surfaces are disturbed strongly in the region of transition, so that the potential surfaces for the initial and product state cannot be separated any more and an adiabatic transition from U_a(q) to U_b(q) takes place.
- For smaller V, the states of $(D^* - A)$ and $(D^+ - A^-)$ do not effectively mix any more. A transition between the potential surfaces U_a(q) to U_b(q) is a statistical process depending on how often the point of intersection is reached, and on the transition probability proportional to V_2.

Long range ET processes with D-A distances larger than their Van-der-Waals distance can usually be described in the framework of non-adiabatic theory and two regimes for the electronic coupling can be separated.

Direct coupling

If only the tails of the electronic wavefunctions contribute to the overlap integral, the matrix element for electronic coupling can be approximated by an exponential distance dependence

$$V(r) = V_0 e^{\beta R} \tag{1.18}$$

where R is the mean distance between donor and acceptor. The attenuation parameter β is an empirical constant which is, according to studies on the distance dependence of ET processes. Even though the expression contains no explicit temperature dependence, the value of the electronic coupling can change due to temperature dependent conformational changes.

Superexchange coupling

If a molecular bridge B is located between D and A like our case , the interaction between D and A can be drastically increased by mixing of B states into the donor-acceptor coupling. In this *superexchange* model, the states of B are only virtually occupied; therefore also energetically higher states can influence the exchange interaction. First order perturbation theory adds a second contribution V_{SE} to the direct coupling V_{dir}:

$$V = V_{dir} + V_{SE} = V_{dir} + \frac{V_{DB}V_{DA}}{\delta E_B} \tag{1.19}$$

The energy gap between the potential surface of B and the point of intersection of the potential surfaces of D and A enters the equation as δE_B. For large D -A distances, the superexchange contribution can exceed direct coupling by far.

In the framework of non-adiabatic ET, the transition from the initial state $|a\nu\rangle$ to a multiplicity of charge separated states $|b\omega\rangle$ can be treated with first order perturbation theory. The microscopic transition rate $\kappa_{|a\nu\rangle\rightarrow|b\omega\rangle}$ can be derived from Fermi's Golden Rule:

$$\kappa_{|a\nu\rangle\rightarrow|b\omega\rangle} = \frac{2\pi}{\hbar}\sum_{\omega}|V_{a\nu,b\omega}|^2\delta(E_{b\omega} - E_{a\nu}) \tag{1.20}$$

The δ function ensures energy conservation between reactant and product states with energies $E_{a\nu}$ and $E_{b\omega}$.

Due to vibronic excitation, ET transfer does not originate from a single state $|a\nu\rangle$, consequently also the reactant state has to be treated as a multiplicity. Within this multiplicity relaxation takes places on a typical time scale of 100 fs up to a few ps. If this relaxation is fast compared to ET reaction, the ET rate κ can be regarded as a weighted sum of the microscopic rates described in equation 1.20

$$\kappa = \sum_{\omega}\rho_\nu\kappa_{|a\nu\rangle\rightarrow\{|b\omega\rangle\}} \tag{1.21}$$

with

$$\rho_\nu = \frac{e^{\frac{-E_{a\nu}}{\kappa_B T}}}{\sum_\nu e^{\frac{-E_{a\nu}}{\kappa_B T}}} \tag{1.22}$$

with a thermally averaged Franck-Condon factor FC:

$$F.C. = \sum_{\nu}\sum_{\omega}\rho_\nu|\langle X_{a\nu}|X_{b,\omega}\rangle|^2\delta(E_{b\omega} - E_{a\nu}) \tag{1.23}$$

The transition rate for non-adiabatic ET as in equation 1.22 depends on the product of the squared electronic transition matrix element and the

Franck-Condon factor as a thermal mean of the overlap of the nuclear wave functions.

1.1.6 Franck-Condon factor

The Franck-Condon factor describes the response of the nuclear configuration to the ET process with a changed equilibrium situation. It takes into account the vibrational state of the system including the surrounding solvent.

Single mode approximation

How we can see in the previous section he multi dimensional potential surfaces of both states can then be reduced to one dimension and approximated by square potential wells and describe two parabolas, see Figure **??**.

$$U_a(q) = \frac{\hbar\omega}{2} q^2 \tag{1.24}$$

$$U_b(q) = \frac{\hbar\omega}{2} (q - \Delta)^2 + \Delta G \tag{1.25}$$

Δ is the value of the generalised reaction coordinate q for the equilibrium situation the product, assuming q = 0 at equilibrium of the reactant. The difference between the free enthalpies in the potential minimum for both states is the driving force ΔG, which is negative for exoergic reactions. The difference in energy of the product at the point of equilibrium of the reactant $U_b(O)$ and at its own point of equilibrium $U_b(\Delta)$ is the reorganization energy λ.

As a consequence of the Franck-Condon principle the actual change between the potential energy surfaces has to occur at fixed nuclear coordinates (vertical transition). As the transition is radiationless, energy remains conserved (horizontal transition). Both conditions are only met simultaneously at the point of intersection of the parabolas. From this consideration the activation energy can be derived the equation 1.13.

In single mode approximation the Franck-Condon factor in equation 1.23 can be given in an analytical form

$$F.C. = \frac{1}{\hbar\omega} e^{-S(2\nu+1)} I_p \left(2S\sqrt{\nu(\nu+1)}\right) \left(\frac{\nu+1}{\nu}\right)^{\frac{p}{2}} \tag{1.26}$$

with modified Bessel functions I_p of the order p and the dimensionless parameters

$$S = \frac{\Delta^2}{2} = \frac{\lambda}{\hbar\omega} \tag{1.27}$$

$$P = \frac{|\Delta G|}{\hbar\omega} \tag{1.28}$$

and the temperature dependent Bose factor

$$\nu = \left(e^{\frac{\hbar\omega}{\kappa_B T}} - 1\right)^{-1} \tag{1.29}$$

At low temperatures $\kappa_B \mathrm{T} \ll \hbar\omega$, equation 1.23 can be reduced to:

$$F.C. = \frac{1}{\hbar\omega} e^{-S}\left(\frac{S^p}{p!}\right) \tag{1.30}$$

describing temperature independent tunneling from the lowest vibrational reactant state to the isoenergetic vibrational product state.

For high temperatures $\kappa_B \mathrm{T} \gg \hbar\omega$ equation 1.23 evolves in a so-called Marcus equation

$$F.C. = \frac{1}{\sqrt{4\pi\kappa_B T}} e^{-\frac{E_A}{\kappa_B T}} \tag{1.31}$$

This reflects the classical Arrhenius type temperature dependence with E_a as in equation 1.30

Multi mode approximation

The vibrational pattern of complex molecules is only described roughly by single mode approximation. In multi mode approximation, in addition to a mean low frequency mode, a second - also averaged - high frequency mode is considered. The ET process is now also allowed to the nth vibrational state $(D^+ - A^-)_n$ of this high frequency mode. The driving force (ΔG) for these reactions is then lower by n $\hbar\omega$ compared to ET to the lowest vibrational state of the product. The Franck-Condon factor in the high temperature case in this model is

$$F.C. = \frac{1}{\sqrt{4\pi\lambda_S\kappa_B T}} e^{-S_\nu} \sum \frac{S_\nu^n}{n!} e^{\left(\frac{\Delta G + \lambda_S + n\hbar\nu}{4\lambda_S\kappa_B T}\right)} \tag{1.32}$$

with the so-called Huang-Rhys factor

$$S_\nu = \lambda_i \hbar\omega \tag{1.33}$$

In this equation, λ_s denotes the (low frequency) solvent reorganization energy, high frequency intramolecular vibrations enter the Franck-Condon factor via λ_i. The Huang-Rhys factor describes the electron phonon coupling of the high frequency mode. For small coupling S_ν tends to zero and the Franck-Condon factor meets the Marcus relation for single mode approximation as in equation 1.31.

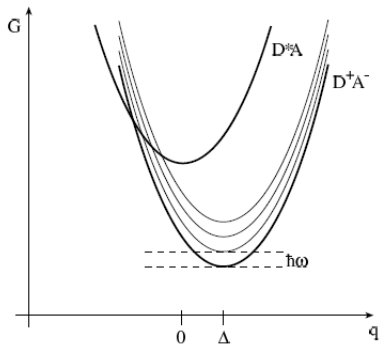

Figure 1.4: High frequency modes in the Marcus inverted .

In the normal Marcus region and in the activationless case, the activation energy for transitions into higher vibronic states is higher as for the lowest vibrational product state. Consequently, the ET rates are comparable in multi mode and single mode approximation. This is not the case in the Marcus inverted region. Here, the transitions to higher vibrational product states are subjected to a decreased activation energy. Therefore, in the inverted region the treatment in multi mode approximation yields higher ET rates than in single mode approximation. Additionally, the dependence of the rate on the driving force and on temperature is lower than in single mode approximation.

1.1.7 Beyond the Born-Oppenheimer approximation: The conical intersection

The Born-Oppenheimer Approximation is the keystone to the visualization of chemical processes. By separating the electronic and nuclear motion, it enables us to picture molecules as a set of nuclei moving over a potential energy surface provided by the electrons. Whereas the validity of this approximation for the vast majority of chemistry is not in doubt, it is now clear that in many important cases the approximation breaks down. The nuclear and electronic motion then couple, and unexpected phenomena may arise.

This breakdown is particularly common in the photochemistry of polyatomic molecules, where there are a large number of energetically close-lying electronic states and many nuclear degrees of freedom. A particularly striking and important example of the result of the coupling between nuclei and electrons, termed vibronic coupling, is a conical intersection between electronic states. Conical intersections, also called photochemical funnels, provide pathways for ultrafast interstate crossing, i.e., on the femtosecond timescale. As a number of publications show, the existence and relevance of such intersections is no longer in doubt. The first demonstration of the effect of a conical intersection on a general, system was made in the study of an unexpected band in the photoelectron spectrum of butatriene.[5]This band can only be explained by a breakdown of the Born-Oppenheimer approximation at the conical intersection connecting two adjacent states. Other similar examples were then found in the photoelectron spectra of molecules such as allene,[6] benzene,[7] and heterocycles.[8] All these cases involve doublet states. An early example in which singlet states are involved was found in the absorption spectrum of pyrazine.[9,10] Here, the band associated with the S_2 electronic state is a diffuse band; a conical intersection with the S_1 electronic state means that the vibronic states in this region of the spectrum have a very short lifetime.

It will be noted that most papers cited in this section are theoretical works. This is because the presence of a conical intersection can usually only be inferred from experimental data, but confirmation requires a study of the relevant potential surfaces. A good example of this is shown by studies on *all*-trans octatetraene. Experimental data showed that a radiationless decay pathway opens up when the molecule has energy above a certain threshold.[11]Calculations then show that this is attributable to a conical intersection that could only be reached along a pathway with a barrier.[12]

An example of the role played by a conical intersection in organic photochemistry is found in the anomalous fluorescence of azulene: The fluorescence is from S_2, rather than S_1. The latter state is coupled to the ground state, and radiationless decay through an intersection occurs instead of fluorescence.[13] Another typical example of the mechanistic importance of conical intersections is found in the cis-trans isomerization of molecules such as butadiene[14] and retinal.[15] Conical intersections also play a role in the unwanted fast relaxation of cyanine dyes.[16] As a final example, a conical intersection is central to the mechanism of the photochromic dihydroazulene/vinylheptafulvene pair. It ensures that the photoreaction only goes in one direction.[17] In all these systems, the intersection is on the pathway from the photoexcited state to the products, and the system is instantaneously transferred back to the ground state after undergoing the initial photochemistry in the excited state.

More direct evidence for a conical intersection can be provided by femtosecond laser experiments. These are able to produce detailed information

about the potential energy surface of a system. Pump-probe experiments have shown,for example, the involvement of conical intersections in the ring opening of 3,3, -cyclohexadiene[18] and the photodissociation of metal hexacarbonyls.[19] Time-resolved photoelectron spectroscopy is also being used to produce detailed information on the non-adiabatic dynamics of a range of systems. Examples include the relaxation dynamics in benzene derivatives, thioxantone,[20] azobenzene isomerization, and proton transfer in hydroxybenzaldehyde.[21] The theory of applying pump-probe experiments to non-adiabatic systems is reviewed in Domcke et all.[22]

Theoretical approach

The total energy $\hat{H} = \hat{T_{nu}}\hat{T_{el}} + \hat{V}(r,R)$ of a molecular system of nuclei (n) and electrons (e) is the sum of their kinetic energy

$$\hat{T}_{nu}(R) = -\frac{\hbar}{2}\sum_n \frac{1}{M_n}\nabla^2 \tag{1.34}$$

$$\hat{T}_e(R) = -\frac{\hbar}{2}\sum_n \frac{1}{m_e}\nabla^2 \tag{1.35}$$

respectively and the potencial energy $\hat{V}$(r,R) of the system, which depends on the electronic r and nuclear coordinates.

To simplify the Schrodinger equation $\hat{H}\Psi(r,R) = E\Psi(r,R)$ for a molecule with wave function Ψ(r,R) Born and Oppenheimer considered that the nuclei are much slower than the electrons, due to their much larger mass. Since the latter can rapidly adjust to every newly acquired position of the former, Born and Oppenheimer (BO) treated the nuclear and electronic motion separately, independent of one another, approximating the molecular wave function as $\Psi(r,R) = X(R)\Psi(r,R)$, where X(R) and $\Psi(r,R)$are the nuclear and electronic wave functions respectively; X(R)depends only on the nuclear coordinates R while $\Psi(r,R)$ depends on the electronic coordinates r and the parametrically on R. Using the method of the separation of variables and within the BO approximation, the Schrödinger equation becomes

$$[\hat{T}_{el}(r) + \hat{V}(r,R)]\Phi(r,R) = \varepsilon(R)\Phi(r,R)X(R) \tag{1.36}$$

$$[\hat{T}_{nu} + \varepsilon(R)]X(R) = EX(R) \tag{1.37}$$

From Eq. 1.37 the eigenvalues of the electronic energy ε for every different nuclear geometry are derived; ε is a function of $f = 3N-6$ internal coordinates (3N-5 for a linear molecule) and constitutes an f-dimensional surface, the potential energy surface (PES).

Once the electronic energy as a function of R is known, it is usually assumed that the molecular vibrations are separable from one another, i.e.

that the vibrational wave function is of the form

$$X(R) = \prod_{k=1}^{f} X_k(R_k) \qquad (1.38)$$

where X_k denotes the vibrational wave function of the normal coordinate R_k . This is in particular possible in the harmonic oscillator approximation.

The conical Intersection

Separating the nuclear from the electronic motion allows us to think of the heavy nuclei moving slowly over a potential energy surface representing the electronic energy; we speak then about adiabatic electronic potentials, energetically well separated. However, when the potential surfaces come close enough, the BO approximation breaks down because then the nuclei and the electrons move at similar speed, so that their motions couple and cannot be treated independently of each other. In these cases the operator $\hat{T}_{nu}(R) = -\frac{\hbar}{2}\sum_n \frac{1}{M_n}\nabla^2$ of the nuclear kinetic energy operates not only on the nuclear wave function $\times(R)$ but also on the electronic wave function $\Phi(r,R)$ and terms proportional to $\langle\Phi_j|\nabla_n\Phi_i\rangle$ and $\langle\Phi_j|\nabla_n^2\Phi_i\rangle$ must be included in the nuclear Schrödinger equation reflecting the fast changes of the adiabatic electronic states with the nuclear coordinates in the vicinity of a particular nuclear configuration. In other words, these 'non-BO' terms indicate that changes of the electronic and nuclear coordinates r and R (i.e. the electronic and nuclear motion) take place within the same time scale and influence each other; the nuclei are now no longer thought of as confined to move periodically in one adiabatic surface and their motion evolves on more than one potential instead. This non-adiabatic interaction depends inversely on both the nuclear masses (the heavier the nuclei the more adequate the BO adiabatic approximation is for the description of the molecular system) and the energy gap between the surfaces.[23] This coupling of the nuclear and electronic motion is termed vibronic interaction.

An important example of the vibronic interaction is a conical intersection (CI) between different potential energy surfaces. A CI is formed when two *f*-dimensional electronic potentials touch (intersect) in some region of the nuclear configuration space, in the vicinity of which the vibronic coupling terms are very large, due to the energetic proximity. The CI space (in which the electronic states are degenerate) is of *f*–2 dimensions; in the remaining two dimensions, which span the branching space, the degeneracy of the potential surfaces is lifted and the crossing is at least weakly avoided.

Figure 1.5 gives a good physical intuition for the role that CI's play in photophysics and photochemistry. The upper cone serves as a collection funnel; it collects population on the upper surface and guides it to the 'outlet' (the tip of the cone) and from there to the lower surface. The intersection point, i.e. the (*f*–2)-dimensional space, is no bottleneck , because the

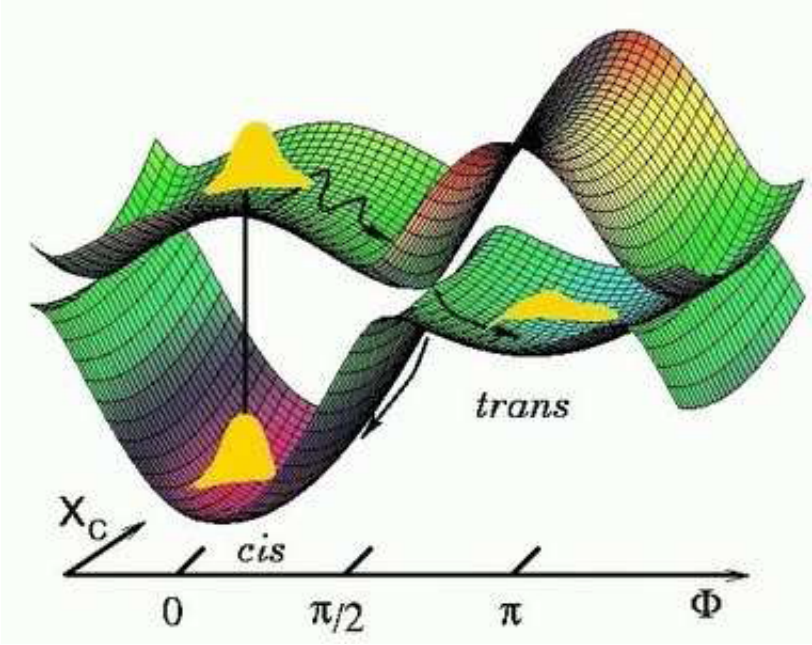

Figure 1.5: A two state model with two vibrational models Coordinate dependent non-adiabatic couplings lead to conical intersection. One can solve the quantum dynamics exactly.[24]

wave packet can also cross over around the intersection point; the crossing needs a time less than a vibrational period.[25,26] The lower cone of the CI constitutes the branching region of the reaction path, where the molecules in fact decide to either return back to the state of the reactant (internal conversion) or to follow the channels towards the reaction products; the relative quantum yields are mainly determined here. The branching space is obviously crucial for the fate of the reaction, so that the CI plays a central role in photochemistry. The other way around, from the spectrum of the products one can sometimes infer the coordinates of the branching space.

For the two coordinates (x_1, x_2) of the branching space one can choose $x_1 = \partial(\varepsilon_1 - \varepsilon_2)/\partial T_k$ and $x_2 = \langle \Phi_1 | \partial \Phi_2 / \partial R_k \rangle$ where $\Phi_{1,2}$ are the adiabatic electronic wave functions of the two intersecting potential surfaces of energy $\varepsilon_{1,2}$ [68] and the integration is performed over all the electron coordinates. The vector of x_1 points to the direction along which the difference in the slopes of the two intersecting surfaces is the largest, while x_2 to the direction of nuclear displacement (from the cone point) that most strongly mixes the two adiabatic electronic wave functions (i.e. the direction of strongest vibronic interaction).

Symmetry often plays a crucial role in the description and classification of conical intersections.[23,27] Intersections can occur between non-degenerate

electronic states of different or the same symmetry and also in cases where no symmetry is present at all; the former are called symmetry-allowed conical intersections. A very important class of CI are those arising from the Jahn-Teller (JT) effect. According to Jahn and Teller if a nonlinear polyatomic molecule of a symmetric geometry (e.g Oh) is in a symmetry-induced degenerate electronic state (e.g. of E or T symmetry), there are always at least two non-totally symmetric (with respect to the symmetry of the molecule) normal coordinates along which the degeneracy is lifted; the two states energetically split and the symmetry of the system is broken. These two coordinates span the branching space of this 'symmetry-induced' (JT induced) CI. The molecule in its new equilibrium configuration is of lower symmetry and energy than in the 'original' symmetric structure, i.e. in the CI, which would be the energy minimum in the absence of any symmetry breaking. Other types of conical intersections are described in Worth et all[23] and references therein.

2

Spectroscopic Techniques

2.1 Transient Absorption Spectroscopy

2.1.1 Basic Principles

Transient absorption spectroscopy (TAS) is an optical pump-probe time-resolved technique. In general, pump-probe experiments are used to investigate the nature and the evolution of the excited states of molecular species in study. In a transient absorption experiments, a short laser pulse, called pump (or excitation) pulse, excites the molecules, bringing them to the electronic excited state of interest. The time evolution of the excited state is monitored by a second broad UV-visible continuum pulse, i.e. the probe pulse, that is delayed in time in respect to the pump. The change in the sample absorbance ΔA before and after the excitation is the physical quantity that one wants to measure. A pump-probe pulse sequence allows to obtain an excited state absorption spectrum at a certain delay time. By repeating this sequence as a function of the pump-probe delay, it is possible to obtain the dynamical evolution (kinetics) of the transient absorption signal.

2.1.2 Instrumental Apparatus

The experimental instrumentation for femtosecond time-resolved transient absorption spectroscopy has been described in detail in previous reports.[28,29] The most critical part of the pump-probe equipment is the source of pulses. Indeed, it must generate pulses short enough toensure an adequate time

resolution, with an high peak power that allows to tune their frequency by means of parametric amplification. The system is based on a self-modelocked Ti:sapphire laser (Spectra Physics, Tsunami), pumped by an intracavity frequency doubled cw Nd:YVO laser (Spectra Physics, Millennia). The pulses (800 nm, ≈ 70 fs, 82 MHz) emitted by the main oscillator are stretched, amplified and recompressed by a regenerative amplifier (BMI Alpha 1000) to give amplified pulses of ≈ 100 fs, with an average power of ≈ 600 mW at 1 KHz repetition rate. The pulse train is divided into two portions of unequal intensity (≈ 95/5). The more intense one is used to produce the excitation beam. In the present experiments the excitation wavelength of 400 nm was obtained simply by the frequency doubling of the fundamental (800 nm) frequency by means of a BBO crystal. The pump beam at 480 nm was obtained by pumping a parametric amplifier, the TOPAS (Travelling-wave Optical Parametric Amplifier of Super-fluorescence).[30] The parametric amplifier generates two pulses at different frequencies, the signal and the idler, that are continuously tunable from roughly 1100 to 1600 nm and from 1600 to 2400 nm, respectively. The frequencies of signal and idler are determined by the phase-matching angle of the BBO crystal. As most electronic transitions are in the UV-vis spectral range, signal and idler can be doubled or combined with the fundamental, to obtain pump pulses from 800 up to 240 nm. In the experimental section relative to each sample taken into account in this work, the experimental conditions are reported.

The weakest portion of light, 1-2 mW, is focused on a CaF_2 plate to produce spectrally broad ('white continuum'), i.e., containing all wavelengths between 350 and 650 nm. The exact wavelength range depends on the specifications of the white light generation. In alternative, by replacing calcium fluorite plate with sapphire, the near infrared components of the probe spectrum (approximately until 1000 nm) become accessible, to the detriment of the blue side.

The white-light continuum was further split into two parts of equal intensity by a 50/50 fused-silica-Al beam splitter. One part, acting as a probe beam, was spatially overlapped with the excitation beam in the sample, the second part crossed the sample in a different position acted as a reference signal. The beams reaches the sample with a variable delay from the excitation pulse, thanks to a suitable optical delay line, while the reference travels along a shorter path and always strikes the sample before the excitation. The reference beam provides a convenient normalization function for the transient spectrum, significantly increasing the signal to noise (S/N) ratio. The delay of the probe in respect to the pump pulse is determined by the distance traveled in the optical delay line, with a minimum step of 30 μm, corresponding to 100 fs.

The three linearly polarized beams are focused onto the same point of the solution by means of a parabolic mirror in a quasi-collinear geometry. The relative pump-probe polarization angle is set to 54.7∘ with the purpose

of excluding rotational contributions to the transient signal.

Sample's solution is usually inserted in a quartz cell (Hellma) with 2 mm optical path. In our case the cell has been modified from we, joining to this a pieces necessary in order to realized a freeze-pump-thaw cycles. The irradiated volume is refreshed by stirring the sample with a micro magnet inside the 2 mm cell and transient absorption spectra were recorded reducing the repetition rate from 1 KHz to 100 Hz to avoid photo-damage of the sample. All the samples were prepared to have an optical density of approximately 1 at the excitation wavelength. Steady-state absorption spectra of the solutions were measured before and after the experiments to check for possible sample decomposition. All measurements were carried out at room temperature (22 ± 1^o).

The acquisition of the transient absorption signal has been performed by the help of a detection system. the pump and probe beams were spectrally dispersed by a Jobin-Yvon CP 140-1824 spectrometer and detected by a Hamamatsu double linear-array CCD system. The electric signals, obtained by a home made front-end circuit, were converted by the help of a simultaneous two-channels analog to digital acquisition board (ADLINK DAQ-2010), and data acquisition was done by means of a LabVIEW computer program.

2.1.3 Spectral Data

Transient absorption spectroscopy is commonly used to monitor the change of absorbance spectrum following the photoexcitation of molecules. The quantity of interest can be extract from the signal according to the following equation:

$$\Delta A(\lambda, \tau) = -\lg(T(\lambda, \tau)) \tag{2.1}$$

where $\mathrm{T}(\lambda, \tau)$ is the photoinduced or transient transmittance. Similarly to the static transmittance, the transient one is defined as the ratio of the intensity of the probe beam recorded with $\mathrm{I}(\lambda, \tau)$ and without $\mathrm{I}_0(\lambda, \tau)$ the pump pulse and can be calculated by:

$$T(\lambda, \tau) = \frac{I(\lambda, \tau)}{I_r(\lambda)} \cdot \frac{I_r(\lambda)}{I_0(\lambda)} \tag{2.2}$$

The intensity of the probe is always divided to the intensity $\mathrm{I}_r(\lambda)$ of the reference beam, that always interacts with the sample before the excitation process. The last factor is the ratio between the intensities of the two beams without the excitation pulse, i.e. the baseline.

The probe and reference beams are spread in wavelength after the dispersion element and a multichannel detection is achieved, so that the intensity profile of the probe $\mathrm{I}_p(\lambda)$ and of the reference $\mathrm{I}_r(\lambda)$ can be obtained at a

given delay time. In practice, each transient spectrum is acquired in three steps. Shutters are used to orderly block and unblock the pump and probe beams in a sequential exposition of the events. This procedure allows to subtract the scattered light contribution from the overall signal.

- I_p + F_p +I_r + F_r with both pump and probe passing through the sample;
- I_p^0, I_r^0 with only the probe;
- F_p, F_r with only the pump.

The commas separate the contributions of the two channels. When the irradiated sample shows luminescence emission, the intensity acquired by the detector system is not related only to transient phenomena. The detector system collects the light continuously and it is not able to discriminate the light pulses synchronized with the pump excitation from the delayed emissions (fluorescence and phosphorescence). Some part of static fluorescence emitted by the sample propagates collinearly with the probe pulse and it is acquired by the detector system, producing a transient spectrum affected by some fluorescence contribution: the stimulated emission (whose intensity is related to the amount of excited state population and hence to the delay between the pump and probe pulse) and the static fluorescence. To avoid the static fluorescence contribution we performed a third acquisition step with the pump beam only. The fluorescence has different intensities on the detection surfaces of the probe and reference beams: F_p and F_s.

All of this contribution are recorded, then subtracted from the intensity obtained when both pump and probe pulses impinge on the sample. So the calculation of transient transmittance at a given delay time between pump and probe is obtained by applying equation

$$T(\lambda,\tau) = \frac{[I_p(\lambda,\tau)+F_p(\lambda)]-F_p(\lambda)}{[I_p(\lambda,\tau)+F_p(\lambda)]-F_p(\lambda)} \cdot \frac{I_r^0(\lambda)}{I_p^0(\lambda)} \qquad (2.3)$$

First of all, the baseline is acquired to correct any mismatch between the two channels. Indeed, the spectral contents of probe and reference, which are the reflected and the transmitted components of the white continuum by a beam splitter, are never exactly the same. This fact makes unreliable the simple ratio for the $T(\lambda,\tau)$ estimation. It is striking to frequently check the stability of the baseline, the flatness and the point to point intensity fluctuations determine the sensitivity of the detection system. We generally observe that 1000 shots are sufficient to produce a baseline which is flat within a variation of absorbance (Δ A) of $\pm$ 0.002.

In general, transient absorbtion spectra arise from three different contributions: excited state absorption (ESA), stimulated emission (SE) and bleaching (B)

- The first contribution is by ground-state bleach . As a fraction of the molecules has been promoted to the excited state through the action of the pump pulse, the number of molecules in the ground state has been decreased. Hence, the ground-state absorption in the excited sample is less than that in the non-excited sample. Consequently, a negative signal in the DA spectrum is observed in the wavelength region of ground state absorption.

- The second contribution is by stimulated emission. For a two-level system, the Einstein coefficients for absorption from the ground to the excited state (A_{12}) and stimulated emission from the excited to the ground state (A_{21}) are identical. Thus, upon population of the excited state, stimulated emission to the ground state will occur when the probe pulse passes through the excited volume. Stimulated emission will occur only for optically allowed transitions and will have a spectral profile that (broadly speaking) follows the fluorescence spectrum of the excited chromophore, i.e., it is Stokes shifted with respect to the ground-state bleach. During the physical process of stimulated emission, a photon from the probe pulse induces emission of another photon from the excited molecule, which returns to the ground state. The photon produced by stimulated emission is emitted in the exact same direction as the probe photon, and hence both will be detected. Note that the intensity of the probe pulse is so weak that the excited-state population is not affected appreciably by this process. Stimulated emission results in an increase of light intensity on the detector, corresponding to a negative ΔA signal.

- The third contribution is provided by excited-state absorption (ESA). Upon excitation with the pump beam, optically allowed transitions from the excited (populated) states of a chromophore to higher excited states may exist in certain wavelength regions, and absorption of the probe pulse at these wavelengths will occur. Consequently, a positive signal in the ΔA spectrum is observed in the wavelength region of excited-state absorption . Again, the intensity of the probe pulse is so weak that the excited-state population is not affected appreciably by the excited-state absorption process.

- A fourth possible contribution to the ΔA spectrum is given by product absorption. After excitation of the photosynthetic, or more generally photobiological or photochemical system, reactions may occur that result in a transient or a long-lived molecular state, such as triplet states, charge-separated states, and isomerized states. The absorption of such a (transient) product will appear as a positive signal in the ΔA spectrum. A ground-state bleach will be observed at the wavelengths where the chromophore on which the product state resides has

a ground-state absorption.

2.1.4 Transient Absorption Signal in the Time Domain

The transient absorption signal is proportional to the concentration of excited states which absorbs the photons of the probe beam at wavelength λ. Within the linear response regime the signal of a pump-probe experiment, in the time domain and at a wavelength λ, is given by the convolution of the molecular response function with the functions associated to the pump and probe pulses.If s(t) is the signal, R(t) is the molecular response function, $p_1(t)$ and $p_2(t)$ are the functions of the pump and probe pulses, then we can write

$$s(t) = R(t) \otimes p_1(t) \otimes p_2(t) \tag{2.4}$$

where $\otimes$ is the convolution operation defined as

$$a \otimes b = \int_{-\infty}^{+\infty} a(t-t')b(t')dt' \tag{2.5}$$

we can write the equation[?] as

$$s(\tau) = \int_{-\infty}^{+\infty}\int_{-\infty}^{+\infty} p_2(t-\tau)P_1(t-t')R(t')dtdt' \tag{2.6}$$

Considering the associative properties for the convolution operation we obtain

$$g(t) = p_1(t) \otimes p_2(t) \tag{2.7}$$

$$g(t'-\tau) = \int_{-\infty}^{+\infty} p_2(t-\tau)P_1(t-t')dt \tag{2.8}$$

The function $g(t'-\tau)$ is the instrumental function and, considering the convolution theorem, it is given by the crosscorrelation function between the pump and probe pulse We can rewrite Equation[?] as

$$s(t) = R(t) \otimes p(t) \tag{2.9}$$

Hence

$$s(t) = \int_{-\infty}^{+\infty} g(t'-\tau)R(t')dt \tag{2.10}$$

The molecular response function is generally associated with the response of the molecular system to an applied perturbation and, therefore, it contains the information about the temporal evolution of the system itself. Hence, R(t) defines the evolution of the molecular property that we want measure.

Transient absorption provides information about the photophysics and the photochemistry of the sample with a temporal resolution limited by the instrumental function. When the time constants of photophysical and photochemical processes are comparable with the instrumental function, the molecular response function can be obtained by a de-convolution operation on the acquired signal. The former operation assumes the detailed knowledge of the instrumental function's profile.

2.1.5 The Instrumental Function

For a faithful deconvolution of the kinetic profiles, the knowledge of the instrumental function is indispensable. The instrumental function is defined as cross-correlation between pump and probe pulses. However, in order to determine the 'real' function, a suitable experiment should be designed, whilst using the same sample cell in the identical conditions (angle between pump and probe and their diameters, for example) used for the actual measurements. As this is often difficult to obtain, in practice the instantaneous signals appearing in transient absorption spectra can be conveniently utilized.[31] These signals include two-photon absorption (TPA), stimulated Raman gain (SRG) and cross-phase modulation (XPM).[32] TPA and SRG are non-linear effects produced by the short laser pulses with very high pump power density, while the XPM arises from the temporal chirp of the continuum white probe, see section *cross-phase modulation*. The temporal envelope of these signals reproduces the pump-probe cross-correlation function, of the equation 2.10.

In particular, in most cases we determined the instrumental function by measuring the time profile of stimulated gain of the most intense Raman bands of the solvent. For a qualitative description of this phenomenon, we can assume that two photons of appropriate frequencies, spatially overlapped and coincident in time, impinge onto the sample. When the excitation frequency is close to a specific component of the probing white continuum, the emission of a third photon can be stimulated. The stimulated gain energy corresponds to the difference between the molecular ground state and a virtual energy level through which the pump photons are scattered and it is specific for each medium. The Raman wavelength λ_{SRG} and the pump wavelength λ_{EXC} can be related by means of the following expression:

$$\frac{1}{\lambda_{EXC}} - \frac{1}{\lambda_{SRG}} = \nu \cdot 10^{-7} \qquad (2.11)$$

The wavelengths must be expressed in nm, while ν, that is the frequency of an active Raman transition of the molecular system, is in cm^{-1}. SRG does not contain any relevant information about the sample; nonetheless, the plot of the intensity of the Raman signal vs the delay time gives the

pump-probe cross-correlation function.

This method allows to measure the instrumental function, even if indirectly. The measure is accurate only if one refers to a probing wavelength near the Raman signal. As a matter of fact, the temporal resolution is primarily determined by the pulse duration; however, the latter is not the only parameter that one should consider for the instrumental function evaluation. There is another effect that possibly contributes to the broadening of the instrumental function. If the central wavelength of the pump and of the probe are different, the refractive index experienced by the two pulses inside the sample cell is different and hence there is a mismatch of the velocity (GVM) of the two pulses. In other words, the pump and probe pulses travel at different speeds in the medium, and the cross-correlation function broadens. The GVM effect can be analytically evaluated writing the relative delay between the pump and the spectral component of the probe beam as:

$$\Delta\tau(\lambda) = \frac{x}{c} \cdot \Delta n(\lambda) \tag{2.12}$$

where x is the position within the sample and $\Delta n(\lambda)$ is the difference between the refraction indexes experienced by the two beams. In the case of Gaussian pulses, the instrumental function broadening due to GVM can be calculated from:

$$G(t) = \frac{c}{a\Delta n}\left\{erf[a(\tau + \frac{l}{c}\Delta n)] - erf(a\tau)\right\} \tag{2.13}$$

where erf indicates the error function. The a constant is given by

$$a = 2\sqrt{\frac{\ln 2}{\Delta\tau^2_{pump} + \Delta\tau^2_{probe}}} \tag{2.14}$$

where $\Delta\tau$ indicates the FWHM of the pulse. The broadening effect described by Eq[?] is obviously dependent on the probe wavelength. In our experiments we never observed any appreciable variation of the measured instrumental function with the probe wavelength. This leads us to conclude that the GVM effect although present, is small and approximatively constant through the entire probe wavelength range considered, at least for the limited path length of the pulses in our samples (tipically 1 mm). As a consequence we can avoid any further correction, and assume that the measured instrumental function contains also some average contribution of GVM.

2.1.6 Group Velocity Dispersion

By using white continuum pulse as a probe, we are able to record at once a broad range of wavelengths. In practice, the wavelengths composing such a pulse are affected by a significant positive chirp due to group velocity dispersion (GVD). A detailed discussion of this effect can be found in reference.[?] The GVD effect influences the recorded spectral features; a possible method to limit such an inconvenience is to reduce the total amount of optical materials introduced into the beam path. However, for the analysis of the spectra in the first picosecond it is necessary to correct for the spectral artifact produced by this effect. The red components of the white continuum speed over the blue components, so that probing in the two visible regions does not occur at the same delay time. Figure figura gvd shows the TA spectral evolution due to the white light dispersion. It should be noted that the signals evolve from left to right, i.e. from the blue to the red side of the spectra. This evolution has nothing to do with any of the molecular processes occurring after the excitation and can be numerically corrected. In order to better discriminate between this contribution and the transient signal of interest we quantitatively determined the GVD contribution as a function of the wavelength by the construction of the dispersion curve plot for each wavelength register the delay at which the signal due to the XPM appears. The fit of this plot is the following equation :

$$\tau\lambda = -8.150 + 0.039\lambda - 6.52 \cdot 10^{-5}\lambda^2 + 3.77 \cdot 10^{-8}\lambda^3 \qquad (2.15)$$

2.2 Transient Infrared Spectroscopy

The broad, often featureless UV/Vis absorption bands commonly seen for solution phase compounds by transient absorption spectroscopy (TAS), due to the fast dephasing times of electronic transitions in solutions, generally allow little structural interpretation. Absorption bands of different species may significantly overlap, complicating the interpretation of experimental results, especially when the complexity of the reaction increases, due e.g. to the presence of different isomers or to the involvement of numerous electronic states. The much narrower, due to the longer vibrational dephasing times, and localized IR bands provide microscopic information about specific functional groups. With some important exceptions (e.g. the OH stretching band in presence of hydrogen bonding), vibrational line widths are rarely larger than 50 cm^{-1} and values in the range 5–20 cm^{-1} are common. This increases the chances of finding spectral regions where different lines do not overlap. Several major advantages, enabling to derive detailed structural

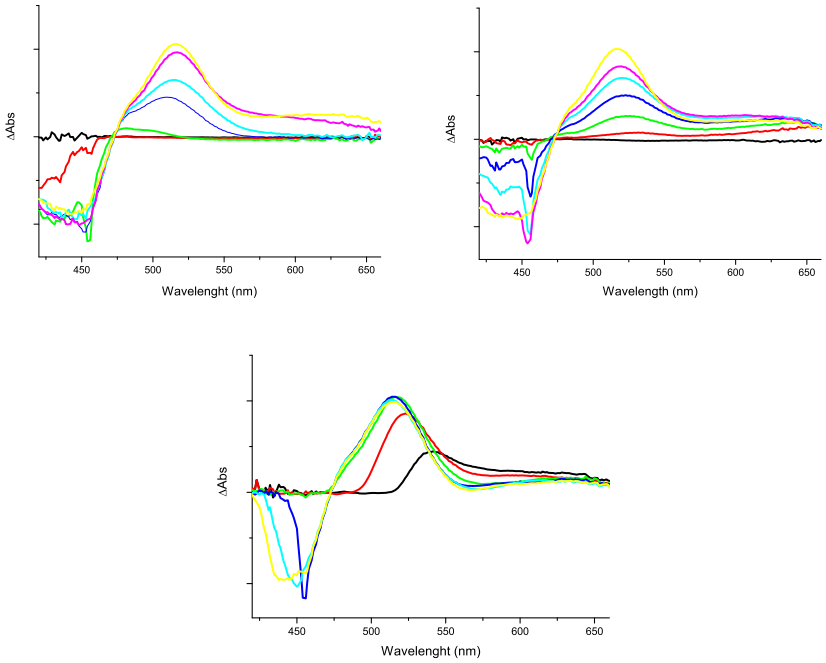

Figure 2.1: TA spectra evolution of a 4AB at shorter delays. The artifact due to the white dispersion follows a spectral evolution that obscures the short-time (hundreds of fs) transient absorption behavior. The experimental data (panel A) are compared to TA spectra after the dispersion compensation (panel B). If the dispersion compensation is overestimate the TA spectra appears deformed (Panel C). The narrow band at roughly 457 nm is the stimulated Raman gain (SRG) signal.

information on molecular geometries are well known:

1. **Site-specific information from inspection of vibrational bands**
   In the case that a molecular vibration is coupled to the reaction coordinate, leading to marked frequency shifts and intensity changes, this mode can be used as spectator for the state of the chemically reactive bond. An important example is given by O-H stretching and O-H bending modes, and C=O stretching modes of hydrogen-donor and -acceptor molecules capable of hydrogen bonding.[33]

2. **Geometric Information from vibrational band patterns**
   Vibrational marker modes can appear, shift or disappear, indicating the occurrence of a rearrangement of nuclear coordinates when crossing occurs from the reactant state to the product state. The combined approach of ultrafast infrared spectroscopy and high-level ab initio quantum chemical calculations allows to gain new insight into microscopic reaction mechanism.

sectionIntroduction Because of the small cross section of vibrational transitions (as compared, e.g. to those of electronic transitions), ultrafast IR experiments are still challenging and only recently, mid-infrared femtoseconds sources were developed which satisfy the technical prerequisites for broad application of ultrafast vibrational spectroscopy.

Generation of tunable femtosecond mid-infrared pulses is usually based on techniques of nonlinear frequency mixing in second order materials. Optical parametric oscillators have been shown to generate mid-IR pulses with nanojoule energies as short as 30 fs. At kHz repetition rates, intense near-infrared pulses, originating from regenerative Ti:sapphire amplifiers, have been used routinely to generate femtosecond (50-150 fs) microjoule mid-infrared pulses in the wavelength range from 2.5 to 20 μm with a variety of conversion schemes.

In this chapter, the experimental setup developed for the ultraviolet pump/mid-infrared probe experiments is described. The laser system is based on a commercial Ti:Sapphire oscillator and regenerative amplifier (Coherent Legend) producing a 1 kHz train of 40 fs, 700 μJ pulses at 800 nm. A small fraction of the light, is diverted with a beam splitter to pump a thin BBO crystal, which produce 400 nm pump pulses. The mid-IR probe pulse is the frequency difference between signal and idler from a home built OPA, and its central wavelength is set to 6 μm.

Laser system

The laser system is a standard kHz Ti:Sapphire amplified system, the Legend Elite, that is a compact Ti:Sapphire regenerative amplifier that delivers pulse energies over 3 mJ at 1 kHz repetition rate, with a pulsewidth < 35 fs and M^2 < 1.35. Legend Elite is a single-stage regenerative amplifier that uses thermo-electrically (TE) cooled Ti:S crystal.

For seeding the Legend-Elite, the oscillator is a Coherent Micra, which delivers broad bandwidth (>100 nm) mode-locked pulses with high average power (300 mW) from a integrated Verdi- 5 W pump laser. To optimize the seeding of any ultrafast amplifier, the Micra presents an adjustable spectral bandwidth (from < 30 nm to over 100 nm) and center wavelength tunability.

2.2.1 Nonlinear parametric conversion

Femtosecond laser pulses are commonly generated in the solid state material Titanium-Sapphire (Ti:Sapphire) and operate in the near-infrared region around 800 nm. However, for many experiments other wavelengths towards the ultraviolet, visible or mid-infrared are required for exciting and probing the molecular system under study.

When intense light interacts with nonlinear materials, nonlinear optical phenomena will appear.[34] Among these effects there are some particularly important at practical level: those which allow light to generate new frequencies, and thus to extend the spectrum of known laser frequencies to the desired mid-IR and UV range. The basis process is a second order nonlinear optical process and require solid state materials with a nonvanishing second order nonlinearity ($\chi^{(2)}$). In practice when two waves at frequencies ω_1 and ω_2 propagate through a nonlinear crystal, a third wave at frequency ω_3 is generated by the $\chi^{(2)}$ process.

This process is called sum frequency generation (SFG) when the generated frequency is $\omega_3 = \omega_1 + \omega_2$. When $\omega_1 = \omega_2$ we have second harmonic generation (SHG). In difference frequency generation (DFG), pulses at $\omega_1 = \omega_3 - \omega_2$ are generated from two input pulses at ω_3 and ω_2.

Another important nonlinear interaction is optical parametric generation (OPG). In this process, a pump pulse at frequency ω_3 generates, in a nonlinear crystal, two new pulses at ω_1 and ω_2 (*idler* and *signal*), starting from quantum noise. If in addition, a weak seed pulse at frequency ω_1 or ω_2 is present together with the pump, there will be an amplification of the signal or idler, which constitutes the optical parametric amplification (OPA). The efficiency of the parametric generation depends on the relative phase an direction of the interacting pulses, which is the *phase matching condition*. The phase matching can be realized either collinearly (scalar phase matching), or non collinearly (vector phase matching). In the collinear case, the phase matching condition is:

$$\mathbf{k_3} = \mathbf{k_1} + \mathbf{k_2} \qquad (2.16)$$

or

$$\omega_3 n_3 = \omega_1 n_1 + \omega_2 n_2 \tag{2.17}$$

where $|\mathbf{k_1}| = n_1 \cdot \left(\frac{\omega_1}{c}\right)$.[1]

The $\chi^{(2)}$ processes can not happen in symmetric media. In birefringent crystals[35] this condition can be satisfied using different polarizations for the interacting pulses. The most commonly used crystal in OPG-OPA setups is the $\beta - BaB_2O_4$ (BBO). BBO crystal has a high damage threshold and supports large bandwidth, so it is a good candidate for parametric generation with intense femtosecond pulses. When it is pumped with the fundamental Ti:sapphire wavelength, it is able to generate frequencies covering the range from 1 μm to 3 μm. the frequency tuning is achievable through the phase matching condition Eq. 2.17: the pair of signal and idler ω_1 and ω_2 can be tuned continuously changing indices n_1, n_2 and n_3, controlling the crystal orientation, the temperature, pressure or electric field applied to the crystal.[36]

2.2.2 Femtosecond mid-infrared pulses

Mid-infrared pulses are obtained in two steps:

1. In the first step, by optical parametric amplification, the pulses from the laser are converted into near-infrared signal and idler pulses ($\lambda_s \approx 1.2\mu m$, $\lambda_i \approx 2.4\mu m$).

2. In the second step, the mid-IR pulses are generated by difference frequency generation in a $AgGaS_2$ crystal.

Our home-made OPA (Fig. 2.2) works in two stages: pre-amplification and amplification of the signal and idler generated into a type II BBO crystal that is seeded by single filament white light. The seeding white light is generated by focusing a portion of the amplified 800 nm pulses into a sapphire plate.[37] The white light is then recombined with the 10 % of the pump pulse onto the BBO crystal. The two beams are spatially and temporally overlapped. The light generated in this first pre-amplification process contain both signal and idler.

For the second amplification step, the undesired idler and residual 800 nm components are removed with dichroic mirrors. The remaining signal beam is sent again onto the crystal and overlapped spatially and temporally with the intense pump beam coming from the laser. the signal and idler are continuously tunable in the wavelength range from 1.2 to 2.4 μm, adjusting the phase match angle. It is important to notice that the type II phase matching guarantees the perpendicularity of signal and idler polarizations, thus

[1] c: vacuum light velocity

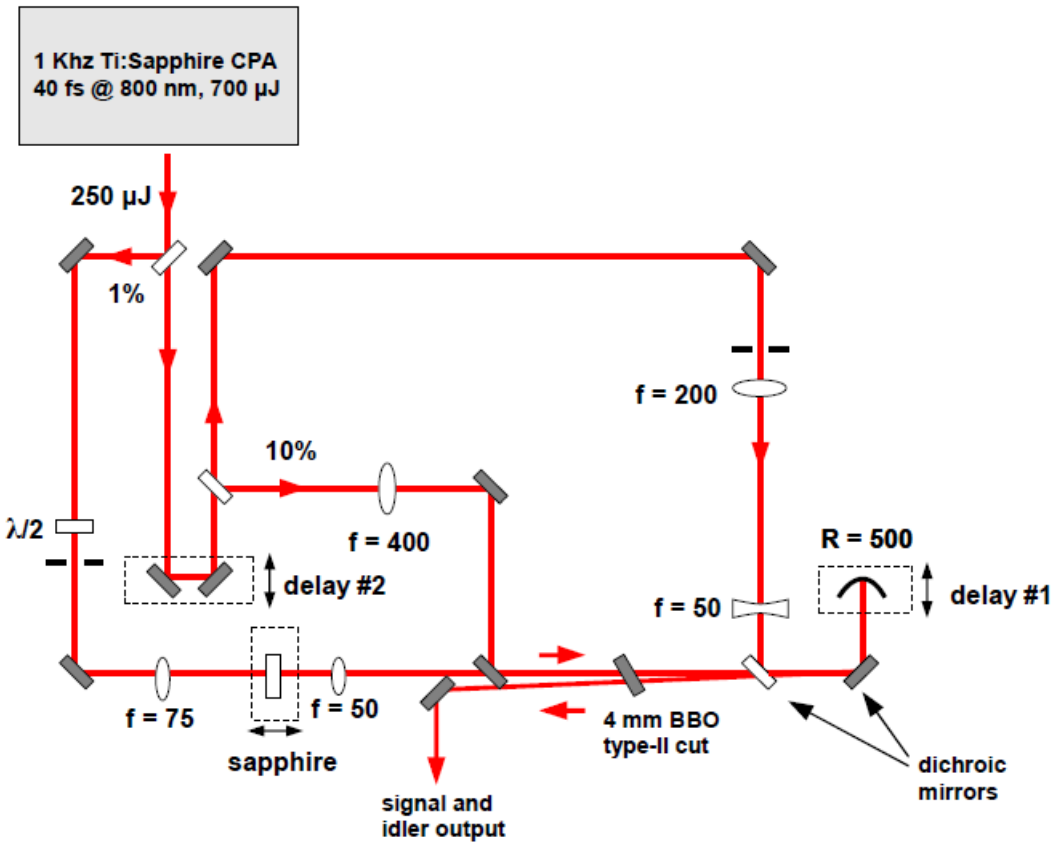

Figure 2.2: Two stages OPA for the generation of tunable femtosecond and idler pulses

they are already correctly aligned for the subsequent difference-frequency process.

In the second step of the light conversion, signal and idler are separated by dichroic mirrors and recombined into a $AgGaS_2$ crystal.[38] The mid-IR pulses are obtained by difference-frequency generation of signal and idler. The pulses are tunable in a wide spectral range from 3 to ~ 10 μm.[39] The energy achieved from a mid-IR pulse is around $1-2\mu$J, with a time duration of $100-200$ fs and bandwidth of 200 cm^{-1}, that covers all the transitions of interest.

2.2.3 Femtosecond UV-Vis pulses

Electronic excitation have been performed using femtosecond pulses at 400 nm. The excitation pulses have been generated by second-harmonic gener-

ation (SHG) a small fraction of the fundamental 800 nm pulses from the commercial Ti:Sapphire oscillator and regenerative amplifier in a type I $\beta - BaB_2O_4$ (BBO) crystal, cut under 29.1° with 100 μm thickness. The pump beam passes through a half-wave plate controlling the polarization and through a telescope in order to reduce the beam diameter, thus the adjustment of the beam diameter at the sample position is facilitated.

2.2.4 Pump-probe setup

The setup for the experiment is essentially a conventional pump/probe setup (Fig. 2.3). The intense ultrashort IR pulse from the OPA is split into pump and probe beams, by means of a beam splitter. The mid-IR pump pulse, which is not used in the UV-pump/mid-IR probe experiment, is then blocked. The recollimated probe pulse pass through a BaF_2 wedged plate which splits off two weak reflections used as probe and reference beams.

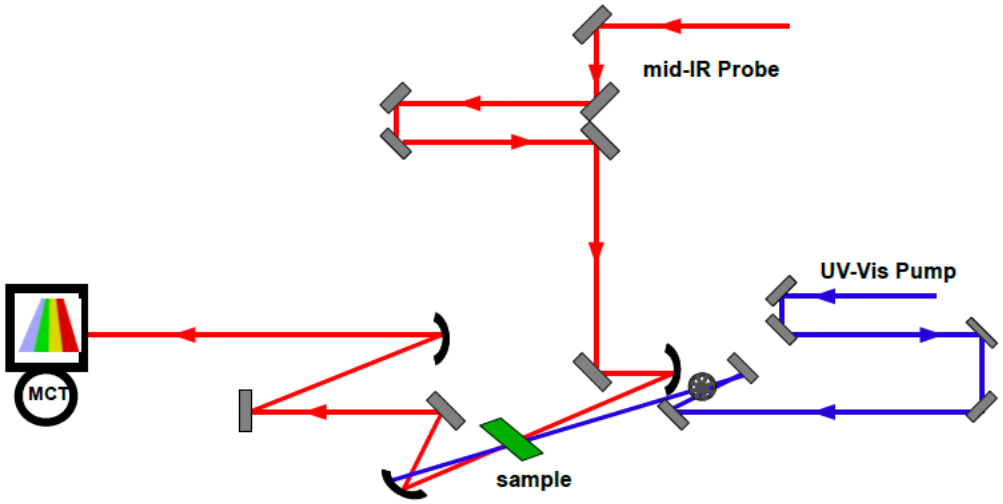

Figure 2.3: Experimental pump/probe setup

The 400 nm pump pulses, generated by SHG in a type I BBO crystal, passes through a computer controlled delay line and is sent onto the sample together with the probe beam. The signal and reference beams are focused by a 30°off-axis parabolic mirrors into the sample, where pump and probe are spatially overlapped, whereas the reference beam crosses an area of the sample not perturbed by the pump. After the sample, the light is collimated and the pump beam is blocked. Finally, the probe and the reference are spectrally dispersed in a grating spectrometer and complete spectra are recorded simultaneously for each shot using a liquid nitrogen cooled double

array (2×32 pixels) of MCT detector.

The sample is maintained between two CaF_2 windows, separated by a spacer whose thickness is chosen depending on the absorbance of the sample. The two windows are mounted on a holder whose position can be varied with three manual linear stages, in order to position the sample in the focus of the crossed beams.

The pump pulse is chopped at a frequency that is half of the repetition rate of the laser (500 Hz), in order to eliminate long term drifts effects, allowing a comparison of the probe intensity with and without pump pulse on two subsequent shots. In this way, it is easy to measure the transient absorption signal normalizing the change of absorbance with respect to the transmission of the reference pulses, and comparing on two subsequent shots with the unexcited case:

$$\Delta A = \log\left[\left(\frac{I_{\text{probe}}}{I_{\text{reference}}}\right)_{\text{pump on}}\left(\frac{I_{\text{reference}}}{I_{\text{probe}}}\right)_{\text{pump off}}\right]\cdot 1000 \qquad (2.18)$$

To avoid spectral and temporal distortion of the mid-IR laser pulses due to the absorption of water vapor and CO_2, the whole pump/probe setup is purged with nitrogen gas. Significant pulse distortion of the infrared pulses is expected at frequencies where gaseous components of air have resonant transitions (3700 cm^{-1}: stretching modes of H_2O; 1600 cm^{-1}: bending mode of H_2O; 2300 cm^{-1}: stretching mode of CO_2). In standard atmospheric air, propagation on distances of the order on several tens of cm produces dramatically distorted pulses, with long trailing wings due to the resonant interaction.[40]

For reference purposes, the sample is replaced by a polished semiconductor (gallium arsenide: $GaAs$) window to determine the zero delay point and to control the pulse duration.

2.2.5 Cross Phase modulation

When performing UV pump/mid-IR probe experiments one must be aware of the artifacts deriving from the non-linear response of the solvent and of the sample cell itself. Cross phase modulation (XPM) is observed when a strong pump pulse modulates the refraction index seen by the probe. The effect is enhanced when the probe pulse is chirped and causes the distortion of the transient signal in both the frequency and the time domains. We undertook a detailed simulation of XPM in the mid-infrared region and in close conditions to the experimental ones. Our simulation takes into account the different group velocities of the pump and probe pulses and includes the influence of the linear chirp of the mid-infrared pulse and its asymmetry. The results of our numerical calculations fit very well the experimental signals

measured in a 2 mm thick CaF_2 window.

When an ultrashort pulse propagates through a medium, it distorts the electronic distribution of atoms and molecules and as a consequence modify temporarily the refractive index seen by the pulse itself.[41] This process induces a time modulation of the pulse phase and generates new frequencies. The pulse phase modulation can be generated by the pulse itself and the phenomenon is defined self-phase modulation (SPM). It can be also generated by a copropagating pulse and cross-phase modulation (XPM) is observed.

In a typical transient absorption experiment, two ultrashort laser pulses (pump and probe) overlap spatially and temporally into a sample. The response, developed by the excited sample, is monitored by measuring the relative absorption changes of a broadband probe pulse as a function of the time delay between the pump and the probe pulses. In experiments with middle infrared (mid-IR) probe pulses the sample thickness is a fraction of that of the windows and the length of the spatial overlap between pump and probe is greater than that. Therefore signals originates mainly from the cell windows rather than from the sample contained within them. XPM, as any other off resonance signals, produced during the temporal overlap of the two pulses, may have an intensity comparable or even stronger than the signal itself, thus seriously modifying the spectral and temporal profiles of the signal to be measured. If one needs to analyze in the first picosecond the spectral evolution due to the sample itself, it is necessary to evaluate the contribution of SPM and XPM.

Being off-resonance processes, the total energy of the probe remains constant during the propagation but it is distributed on different frequencies. The probe spectrum is broadened and the pulse envelope develops an oscillatory structure. We utilize a simplified model where SPM can be neglected because the probe pulse is less intense than the pump.

The propagation of an optical wave through a non-linear medium is described by the wave equation, that is a scalar equation if both pulses are linearly polarized:[42,43,44]

$$\nabla^2 E' - \frac{1}{c^2}\frac{\partial^2}{\partial t^2}(n^2 E') = 0 \qquad (2.19)$$

where E' is the total electric field and c is the light velocity in vacuum. The refractive index, as function of the frequency, presents a linear part n_0 and a non-linear part that depends on the intensity of the total electric field impinging on the sample:[42,43]

$$n(\omega) = n_0(\omega) + n_2 I \qquad (2.20)$$

where $n_2 = 3\chi^{(3)}/8n_0$ is the non-linear refractive index.[45] The frequency

dependence of the linear part of the refractive index is responsible for the group velocity dispersion (GVD). If we represent the electric field of a pulse as:

$$E(x,y,z,t) = \Re\left(F(x,y)A(z,t)e^{i(\omega t - kz)}\right) \tag{2.21}$$

we can define the group velocity as:

$$v_g = \left[\frac{dk}{dw}\right]^{-1} \tag{2.22}$$

and the GVD coefficient as:

$$\beta^{(2)} = \frac{d^2k}{dw^2} \tag{2.23}$$

The GVD effect comes out from the frequency dependence of the linear part of the refractive index. The non-linear effects are included through the parameter n_2 that, in general, can be considered as a constant in respect to the frequency. The intensity is the squared module of the total electric field $I = |E|^2$, where the total electric field is:

$$E'(x,y,z,t) = \Re(F_{pu}(x,y)A_{pu}(z,t) \times exp[i(k_{pu}z - \omega_{pu}t)] + F_{pur}(x,y)A_{pr}(z,t) \times exp[i(k_{pr}z - \omega_{pr}t)]) \tag{2.24}$$

where ω_{pu} and ω_{pr} are the optical frequency of the pump and probe pulses, $k_{pu} = n_{pu}\omega_{pu}/c$ and $k_{pr} = n_{pr}\omega_{pr}/c$ are the wave vectors, and $n_{pu} = n(\omega_{pu})$ and $n_{pr} = n(\omega_{pr})$ the linear refractive index at the carrier frequencies. $F_{pu}(x,y)$ and $F_{pr}(x,y)$ describe the transverse distributions of the two fields; they play a role in calculating the overlap integral. This transverse distributions are in general different for two pulses because of the difference in the center wavelengths, nevertheless the differences among various overlap integrals are small and an effective cross sectional area A_{eff} is introduced.[43]

At this point, we can substitute the expression of the total field into the wave equation. In order to make life simpler it is possible also to apply the slowly-varying-envelop approximation, and expand k_j in a Taylor series around the respective central frequencies up to the second order. In this

contest, the derivation of the coupled-amplitude equation is easy:

$$\frac{\partial}{\partial z}A_{pu}(z,t)+\frac{1}{v_{gpu}}\frac{\partial}{\partial t}A_{pu}(z,t)+\frac{i}{2}\beta_{pu}^{(2)}\frac{\partial^2}{\partial t^2}A_{pu}(z,t)=$$

$$i\gamma_{pu}\left(|A_{pu}(z,t)|^2+2|A_{pr}(z,t)|^2\right)A_{pu}(z,t)$$

$$\frac{\partial}{\partial z}A_{pr}(z,t)+\frac{1}{v_{gpr}}\frac{\partial}{\partial t}A_{pr}(z,t)+\frac{i}{2}\beta_{pr}^{(2)}\frac{\partial^2}{\partial t^2}A_{pr}(z,t)=$$

$$i\gamma_{pr}\left(|A_{pr}(z,t)|^2+2|A_{pu}(z,t)|^2\right)A_{pr}(z,t) \qquad (2.25)$$

where the nonlinearity coefficients $\gamma_j=\frac{n_2\omega_j}{cA_{eff}}$ are introduced. The first terms in the right-hand side of the equations represents, respectively, the SPM of the pump and of the probe, while the second terms are, respectively, the XPM induced into the pump by the probe and vice versa. In the case of a pump-probe configuration, it is possible to reduce the equations making some approximations:

- (i) when weak probe pulses are used, their SPM contribution can be neglected, as well as the XPM induced into the pump by the probe.

- (ii) the sample thickness (a 2 mm thick CaF_2 window) is short in respect to the dispersion length, this mean that the GVD effects are negligible, $\beta_{pu}^{(2)}=\beta_{pr}^{(2)}=0$

The equations are then reduced:

$$\frac{\partial}{\partial z}A_{pu}(z,t)+\frac{1}{v_{gpu}}\frac{\partial}{\partial t}A_{pu}(z,t)=i\gamma_{pu}|A_{pu}(z,t)|^2A_{pu}(z,t)$$

$$\frac{\partial}{\partial z}A_{pr}(z,t)+\frac{1}{v_{gpr}}\frac{\partial}{\partial t}A_{pr}(z,t)=i2\gamma_{pr}|A_{pu}(z,t)|^2A_{pr}(z,t) \qquad (2.26)$$

It is convenient to evaluate the solutions of equations 2.26 in a new coordinate system (z,τ) moving with the group velocity of the probe pulse and normalized to its time duration τ_{pr}:[43]

$$\tau=\frac{t}{\tau_{pr}}-\frac{1}{\tau_{pr}}\frac{z}{v_{gpr}} \qquad (2.27)$$

In this reference frame the coupled amplitude equations take the follow-

ing form:

$$\frac{\partial}{\partial z}A_{pu}(z,\tau) = i\gamma_{pu}|A_{pu}(z,\tau)|^2 A_{pu}(z,\tau)$$

$$\frac{\partial}{\partial z}A_{pr}(z,\tau) + \frac{\epsilon}{L_W}\frac{\partial}{\partial t}A_{pr}(z,\tau) = i2\gamma_{pr}|A_{pu}(z,\tau)|^2 A_{pr}(z,\tau) \qquad (2.28)$$

where $\epsilon = sgn(v_{gpu} - v_{gpr})$ and $L_W = \frac{\tau_{pr}}{|v_{gpu}^{-1} - v_{gpu}^{-1}|}$ is the walk-off length. For such a system it is possible to calculate an analytical solution. XPM and group velocity mismatch are taken into account while higher order effect due to GVD broadening are not considered. The general solution evaluated at the end of the sample $z = L$ is:

$$A_{pu}(L,\tau) = A_{pu}\left(0, \tau - \epsilon\frac{L}{L_W}\right)e^{i\phi_{pu}}$$

$$A_{pr}(L,\tau) = A_{pu}(0,\tau)e^{i\phi_{pr}}$$

$$\phi_{pu}(\tau) = \gamma_{pu}L|A_{pu}(0,\tau)|^2$$

$$\phi_{pr}(\tau) = 2\gamma_{pr}\int_0^L \left|A_{pu}\left(0, \tau - \epsilon\frac{z}{L_W}\right)\right|^2 \mathrm{d}z \qquad (2.29)$$

The XPM contribution changes along the sample because of the group velocity mismatch (GVM) and it is obtained by integrating along the sample length L. In order to perform the integration it is necessary to give a specific shape to the two pulses. These are the initial conditions. Simulations have been performed for different initial conditions. The pump pulse in all the cases is represented by an unchirped gaussian pulse delayed in time in respect to the probe pulse:

$$A_{pu}(\tau) = A_{0pu}e^{-\frac{4\log 2}{\tau_{pu}^2}(\tau+\Delta T)^2} \qquad (2.30)$$

ΔT is the delay time between pump and probe. In the calculus two types of probe pulses have been considered: a chirped symmetric gaussian pulse and a chirped asymmetric pulse.

Thus, as is shown in Fig. 2.4, in order to reproduce the experimental XPM it is necessary to utilize asymmetric pulse envelopes with chirping. By adjusting these two parameters it is possible to perfectly fit the experimental time curves. At present, the parameters are evaluated in an empirical way. However a global fitting program is under construction. Therefore, it will be soon possible to extract all the characteristic properties of MIR pulses directly measuring the XPM effect on the cell sample itself, without

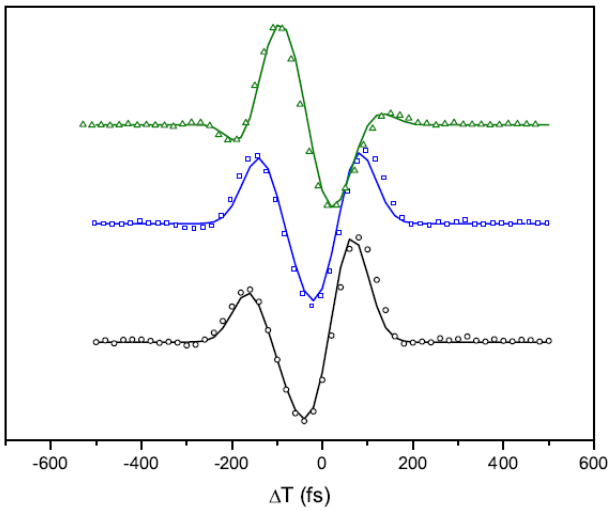

Figure 2.4: Simulation (line) done with an asymmetric chirped probe pulse Chirp 1.8 * 10^{-4}fs^{-2}, τ_{pr} = 120 fs. The open circles are the experimental curves taken at ν = 1608 cm^{-1}, the open squares are the experimental curves taken at ν = 1634 cm^{-1} (at the band center frequency) and the open triangles are the experimental curves taken at ν = 1736 cm^{-1}

introducing additional optical components in the experimental setup.

2.3 Fluorescence lifetimes

The samples are excited by tunable femtosecond pulses obtained from the laser apparatus described for TAS. The fluorescence is collected by a quartz lens and focussed onto the photocathode of a Hamamatsu R2809U-01 microchannel plate photomultiplier, after elimination of the excitation beam scattered radiation, by means of an appropriate set of colored filters. The photomultiplier signal is fed into a digital oscilloscope (2.5 GHz band-pass). The slightly asymmetric instrumental function, measured by light scattering from a latex solution, has a time duration (FWHM) of 550 ps, highly reproducible from one experiment to another. The experimental time profiles were deconvoluted taking into account the instrumental function, and were fitted by exponential functions, obtaining intrinsic fluorescence lifetimes.

2.4 Steady State Spectroscopy

The absorption spectra have been recorded by a Lambda 950 Perkin Elmer model spectrophotometer. The fluorescence spectra were measured by means of a Perkin -Elmer spectrophotofluorimeter (mod. LS55). The FTIR was recorded by a ...

2.5 Experimental Details

Solutions were freshly prepared using ethanol, methanol, deuterated methanol, chloroform and carbon tetrachloride was purchased from Sigma Aldrich all of them spectrophotometric grade.

The solutions changed rapidly color by simply leaving the sample cell in the light of laboratory. The stability of the solutions depends on quantity of oxygen into the solution, for this reason we try to remove the oxygen using different techniques, the first was bubbling an inert gas into the solution, using it the stability of the compounds proved to be a few minutes, enough to make measurements. The combination of bubbling nitrogen with application of ultrasound was also tested with practically identical results, the spectral shape of the compounds changed after few minutes.

The oxygen was finally removed from the solutions by applying several freeze-pump-thaw cycles. The equipment necessary for this kind of process is a home made quartz cell, with a reservoir and with a valve for the vacuum and N_2. Before the freeze-pump-thaw cycles N_2 was bubbled through the solvents, then place the solvent (or solution) in a Schlenk flask, in our case in the special cell, we must ensure that the stopcock is closed, and be careful that not use more than 50% of the volume of the flask because overfilled flask frequently shatter during this process. Hook it up to a cell line (leave the attached hose on vacuum throughout this procedure) and freeze the liquid. Liquid nitrogen was used for this. Before freezing make sure that the environment in the flask is free of oxygen to prevent condensing liquid oxygen upon freezing.When the solvent is frozen, open the stopcock to vacuum and pump off the atmosphere for 10-30 minutes. Seal the cell and then thaw the solvent or solution until it just melts using a tepid water bath. You see gas bubbles evolve from the solution, then replace the water bath with the cooling bath and refreeze the solution, we repeat these steps until gas bubbles are not seen in the solution. After the last cycle the solution was left under a N_2 atmosphere and the valve closed. Whole process has been protecting the solution from light. In this conditions the solutions , kept at room temperature, results stable for several hours. The UV-vis spectra of the solutions were monitored until no further modification was observed.[46,47]

The fluorescence spectra were taken with sample concentration in the

range 10^{-4} 10^{-7} M, no difference has been noticed within the mentioned limits. The quantum yields were estimated by comparison with compounds of well-known quantum yield.[48] In order to avoid any inner filter effects, the absorbance was adjusted not to exceed 0.1 at the absorption maximum. The absorption spectrum at the end of each fluorescence experiment was found to be substantially coincident with the absorption spectrum before experiment. No difference in the fluorescence profiles was noticed varying the concentration within the above mentioned limits. Each solution spectrum was duplicated by that of the solvent alone, devoid of emission bands in the spectral region of interest. Coumarine 120 $\Phi_{S_1 \rightarrow S_0}$ = ???? in ethanol and coumarin 153 $\Phi_{S_1 \rightarrow S_0}$ = 0.42 in methanol solution were used as standards[49] . The integrated fluorescence intensities are linearly proportional to absorbencies. With the same excitation wavelength , quantum yields are obtained from the the simple expression

$$\frac{\Phi_A}{\Phi_B} = \left(\frac{m_A}{m_B}\right)\left(\frac{\eta_A^2}{\eta_B^2}\right) \tag{2.31}$$

where A and B are the two compounds coumarine 120 and coumarine 153, m_A and m_B are the slopes of the A and B linear plots, and η the refractive index of the solvent.

3

Donor-Acceptor System [2DA]

The 2,2′-bipyridine ligand has been extensively used as a metal chelating ligand due to its robust redox stability and ease of functionalization.[50] In contrast to other ligands, such as catechol, which is dianionic, and derivatives of the acetylacetonate ion, which are monoanionic, the 2,2′-bipyridine is a neutral ligand. It thus forms charged complexes with metal cations, and this property has been exploited in the design and synthesis of metal-bipyridine complexes.

The photophysical properties of 2,2′-bipyridine has been widely studied. From picosecond emission experiments and semiempirical calculations have found very short fluorescence lifetimes has been found (~160 ps in cyclohexane and ~ 50 ps in methanol).[51] The lifetime of the S_1 state in various solvent has been studied by subpicosecond transient absorption experiments founding (τ_{S_1} is 70 ps in cyclohexano, 64 ps in acetonitrile, 54 ps in water, 77 ps in methanol and 53 ps in 2-propanol).[52] The lifetime of the lowest triplet state T_1 is 100 μs, this value has been found through transient absorption spectroscopy and time resolved resonance raman (TRRR).[53] Once a donor is bond to the 2,2′-bipyridine the nature of the excited states is complete different. As shown in the Figure 3.1, the molecule is symmetrical, the bipyridine is connected with the donor moiety (2-ethylhexyl pyrrole) by ethylenic units. The schematic structure is a π-Donor-Bpy, in which the bipyridine acts as an acceptor, and pyrrole moiety acts as a donor. Although the IUPAC name of the chromophore is 4,4′-Bis(E)-2-[N-(2-ethylhexyl)pyrrol-2-yl]vinyl-2,2′-bipyridine, for simplicity in this thesis we will denominate it as 2DA.

The synthesis of this dye was performed by Abbotto et al.[54,55]

Some of the photophysical and photochemical properties of this compound make it a good candidate to be studied as a model compound to

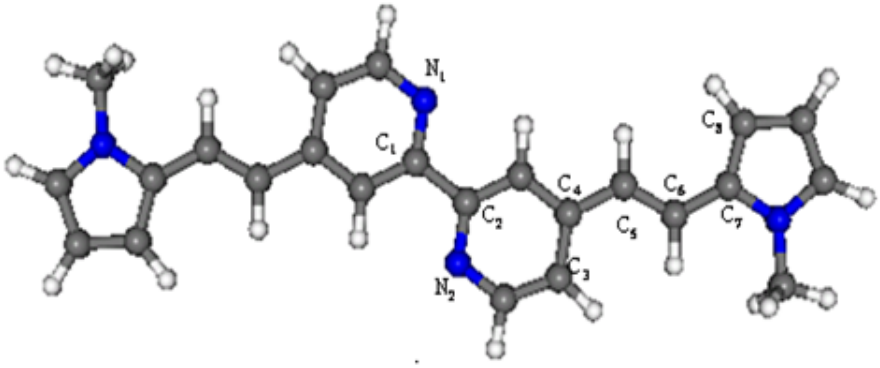

Figure 3.1: Schematic representation of the molecule 2DA

provide insight into the electron transfer process. We can compare its photophysical characteristics with those of the simplest fragment, taken as the division of the molecule 2DA by the middle of bipyridine, in order to evaluate the effects of the linking the two D-A heteroaromatic arms. As expected, a bathochromic effect is present upon linking the monomeric unit in the bipyridine dimer.[56] The maximum of the absorption band for the monomer is centered at 362 nm in methanol with an extinction molar coefficient (ε) of 21900 $mol^{-1}L\ cm^{-1}$. On the other hand, the maximum of the absorption band for the 2DA ligand is shifted to 377 nm, and the extinction molar coefficient is (ε) of 39 000 $mol^{-1}L\ cm^{-1}$, practically doubling to that of the monomer.

In order to achieve more information on possible solvatochromic effects, the authors changed the alkyl chain of the pyrrolic moiety for a tris(ethylene glycol) monomethyl ether chain, showing that this last compound presented a maximum of absorption centered at 374 nm in CH_2Cl_2 (TEG). Since the peripheral chain does not interferes with the π-framework, the differences in the two systems can be mainly ascribed to solvatochromic effects. Because the polarities of the ground and excited state of a chromophore are different, a change in the solvent polarity will lead to differential stabilization of the ground and excited states, and thus, a change in the energy gap between these electronic states. Interestingly, a significant solvatochromic effect (26 nm) is found for the emission spectra, with a redshift upon increasing the solvent polarity, whereas no significant difference is found for the absorption peaks (377 nm 2DA in DMSO vs. 374 nm for the TEG derivative in CH_2Cl_2).

In this chapter we describe the photophysical properties of the ground state and, for the first time, those of the excited state of a simply π-donor-substituted $2,2'$-bipyridine.

3.1 Absorption and Emission Spectra

The measurements of absorption and fluorescence spectra where performed on diluted solutions ($c = 5 * 10^{-6}$ M or less) in ethanol, and are showed in Figure 3.2.

Ground-state UV absorption spectra of the 2DA ligand in ethanol presented an intense intramolecular charge transfer band in the visible region with a maximum at 378 nm and molar extinction coefficient of 39,000 $mol^{-1}L$ cm^{-1}. The fitting process with a Gaussian lineshapes curves was performed to determine the position, widths and relative intensity of individual bands. The number of Gaussian lines used, as well as their parameters, were determined from optimization of a free fit, i.e., without any parameter constraints. The band is clearly asymmetric. Three Gaussian lines were necessary to describe the experimental spectra, centered at 381, 350, and 328 nm, with relative intensities of 2.74, 1 and 0.1 respectively. The agreement between calculated from ab-initio calculations (DFT and TDDFT) and experimental absorption maxima is excellent. The lowest transition, corresponding to the HOMO⟶ LUMO transition at 354 nm, is symmetry forbidden and does not contribute to the absorption spectrum. The HOMO-1⟶ LUMO transition at 362 nm (f= 0.3) and the third-excited state (f=1.64), involving HOMO⟶LUMO+1 transition at 387 nm, dominate the absorption spectrum due to their strong intensity.

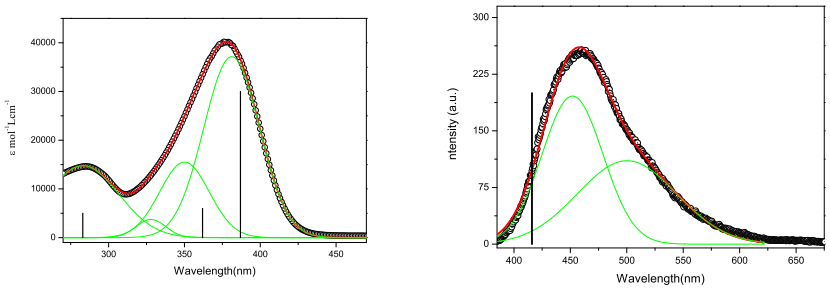

Figure 3.2: Absorption and emission spectra (*black line*) solvent EtOH plotted together with a Gaussian fit (*red*) and individual Gaussians are shows in *green*. The vertical lines are the excitation lines calculated from TDDFT, scaled for the intensity of their eigenvalues.

The absorption measurements were also performed on chloroform and methanol-d4 solutions. The band parameters are listed in Table

The fluorescence emission spectrum, recorded on ethanol solution, presents a band between 380 and 600 nm, with a maximum at 460 nm. Two Gaussian curves were necessary to fit the spectra, centered at 452 and 498 nm respectively, with the same area. This value should be compared to the cal-

culated adiabatic ΔE, which presents a value of 416 nm. The large difference between experimental and calculated fluorescence is taken as an indication of the polarity once performed on the excited states.

In the Figure 3.2 is shown the absorption along with the emission spectrum of 2DA ligand; the Stokes shift, calculated as the difference between the maxima of the absorption and the emission, in ethanol solution has a value of 4760 cm^{-1} whereas in DMSO solution this value increases to 5520 cm^{-1}.[55] The ground-state UV absorption spectra of 2DA ligand, does not seem to be much influenced by the solvent. The maximum of the band is 377 nm in DMSO solution, whereas in ethanol solution is at 378 nm. However, the maximum in the emission spectra, seems to shift from 476 nm in DMSO solution, to 460 nm in ethanol solution. This seems to indicate that the nature of the solvent influence only the excited states of the molecule. This is consistent with the charge transfer nature of the excited state. In fact the charge separation is stabilized in polar solvents.

3.2 Transient Absorption Spectroscopy

Time resolved absorption spectroscopy was used to characterize the dynamics of excited states of the chromophore 2DA. Due to the poor stability of the compound and the difficulty to synthesize it, only measurements on ethanol solution have been made. In the figure X are reported the transient absorption spectra of 2DA ligand in ethanol solution, in the spectral range of 420–650 nm. The TA spectra were recorded at several delay times with respect to the photoexcitation. The excitation wavelength was 400 nm, in resonance with the intramolecular charge transfer transition. The features of these spectra are:

- (i) An intense positive band around 430 nm corresponding to the excited state absorption (ESA), and a weak broad positive band around 600 nm.
- (ii) A weak negative band around 490 nm, corresponding to the stimulated emission (SE).

The rise of ESA band is well described by the convolution of a step function (instantaneous response), with the instrumental function (FWHM 200 fs). The time evolution of the transient absorption signal, measured at 430 nm, is shown in the Figure 3.4. We observe a decay of the signal, which is well fitted with a bi-exponential function whose parameters are: A_1 =0.029 ± 0.001, τ_1 =11.7 ± 0.9 ps, A_2 =0.026 ± 0.001, τ_1 =117.9 ± 8 ps.

The most striking feature is the transient absorption dip evolving into a stimulated emission structure . The time profile recorded at 490 nm corresponding to the stimulated emission (SE), initially is positive then negative.

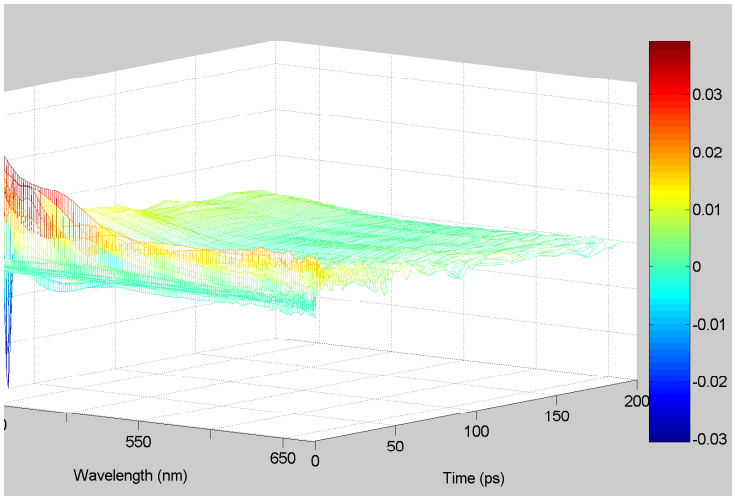

Figure 3.3: Transient spectra recorded after 400 nm pump excitation, of a solution of 2DA (solvent=EtOH, Abs400nm ≃ 0.6).

As shows in the right panel of the Figure 3.4 fit with an exponentially rising response (time constant of 800 fs), convoluted with a pulse duration of 200 fs. Therefore the fluorescence state doesn't form instantaneously.

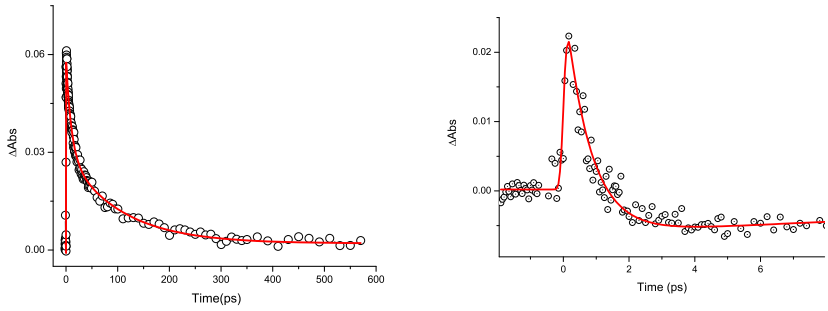

Figure 3.4: Amplitude vs. time profiles for the stimulated emission (490 nm) a short delay times (*right panel*) and transient absorption band (430 nm) of 2DA in ethanol (*left panel*). In *red* the best result of deconvolution/fitting process.

3.2.1 Singular Value Decomposition

We performed single value decomposition (SVD) to the 2DA ligand spectra, in order to estimate the number of spectrally independent components, eliminate random noise, and to store spectral information in a compressed form. The kinetics vectors of the SVD output were fitted by sums of exponentials,

yielding phenomenological rates and amplitudes. Three different spectrally components were found, with evolution time constants of τ_1 =0.68 ps, τ_2 =6.25 ps and τ_3 =119,8 ps . The decomposition procedure gave three main components, characterized by singular values of S_{11} = 2.30 and S_{22} = 0.57 and S_{33} = 0.33. The three DADS obtained with the SVD method are shown in the Figure 3.5 and the corresponding parameter in the Table 3.1.

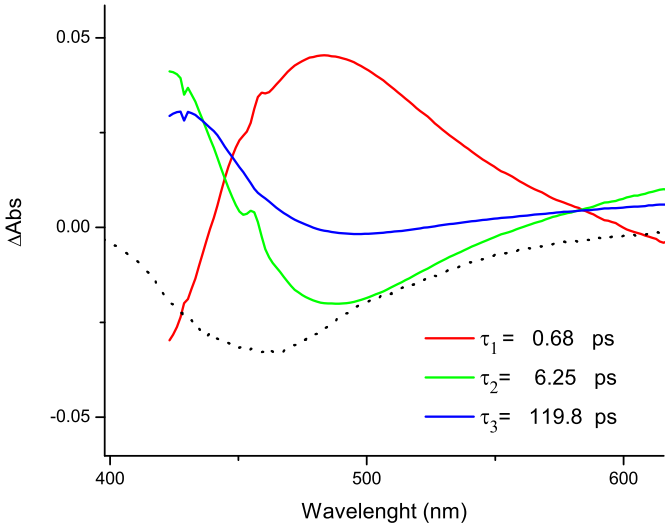

Figure 3.5: Spectral components of the three time contributions to the transient absorption signal in ethanol. $DADS_1$ in *red*, $DADS_2$ in *green* and $DADS_3$ in *blue*. The steady emission spectrum in *dotted line* was plotted along the DADS for a better comparison with the stimulated emission position.

	0.68 ± 0.1 (ps)	6.25 ± 0.4(ps)	119.8 ± 10 (ps)
SV_1	0.004	0.136	0.134
SV_2	0.309	-0.047	-0.014
SV_3	-0.076	0	0

Table 3.1: Parameters for a simultaneous fit of time courses of single value decomposition components with a three exponential model.

In the first picosecond we observe a very large band whose spectral features are a maximun at 483 nm which extends from 440 to 580 nm, can be attributed to a first excited state strongly delocalized. The fast relaxation give origin to a charge transfer state with a localization on the bipyridine

moiety in a hot vibrational state, that through a vibrational cooling relaxes to a excited state and then to the ground state.

3.3 Ab initio Calculations

To gain the insight into the structural, electronic and optical properties of the dye , we performed DFT and Time Domain DFT calculations on system. We optimized the molecular structures of the system without any symmetry constraints using the B3LYP exchange-correlation functional and a 6-31G* basis set. Using the same computational setup, we performed TDDFT calculations of the singlet-singlet excited states at the optimized geometries, in order to simulate the optical absorption and spectrum of the ligand. All the calculations have been performed by the GAUSSIAN 03 program package.[57]

Geometry optimizations were performed considering both a *cisoid* and *transoid* arrangement of the bipyridine, for the ground state and the first excited state. In this case, the *transoid* arrangement was found to be favored being the ground state energy 0,4 eV lower.

For the molecule 2AD the first excited state is originated from a HOMO-LUMO transition that it turned out to be symmetry forbidden. Because of the symmetry of the system, it is expected the same behaviour in terms of geometric relaxation for the dark state and the bright one. HOMO-LUMO excitation transfers charge density from the periphery to the central part of the molecules. In particular, the ground and the first excited states of the analyzed systems involve the population of a anti-bonding orbital between C_5-C_6, while a bonding one between C_4-C_5 and C_1-C_2.

In line with the discussion of the electronic states, the geometrical parameters subject to greater variation in the transition from the ground to the excited state are the length of the double bond C_5-C_6 that increase of 0.03 Å; and the C_4-C_5 and C_6-C_7 that decrease of 0.4 and 0.2 Å respectively. Another length bond that decreases is the bond of the central carbons of the bipyridine. The excited state presents a loss of symmetry in comparison to the ground state so that the main geometric variations are registered in a single side of the molecule. The asymmetry of the excited state is confirmed by the variation of the angle between N_1-C_1-C_2, that increases in S_1 in relation to the ground state.[1]

The Table **??** gives comparisons between the geometric parameters optimized for the ground state (S_0) and for the first excited state (S_1).

[1] The numbering of the atoms can be found in Figure 3.1

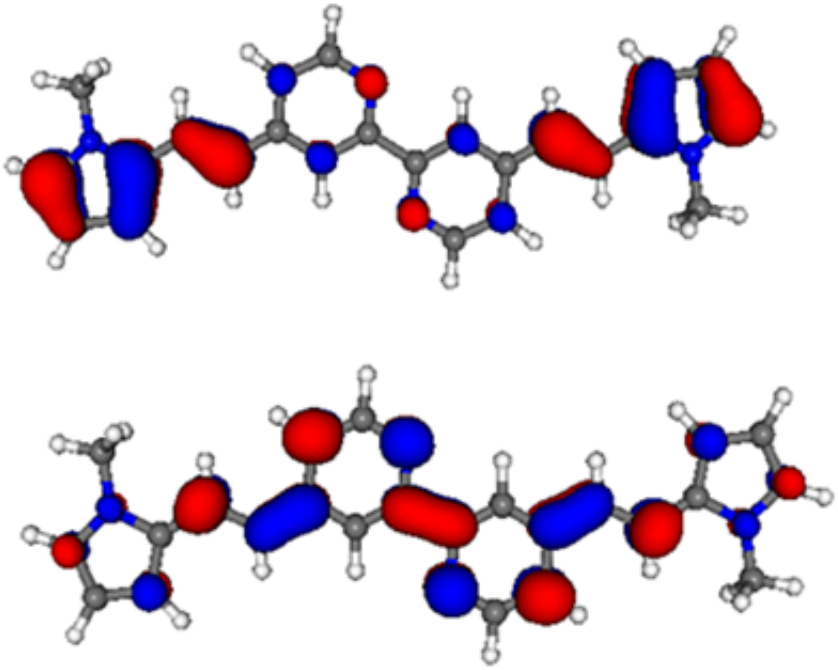

Figure 3.6: HOMO and LUMO orbitals calculated by TDDFT.

3.4 Steady State FTIR Spectra

The assignments:... The steady-state spectra are assumed to contain contributions from only the ground state.

3.5 Time-Resolved Infrared Spectroscopy

Mid-IR characterization of the 2DA excited states could provide new insights to understand the nature the long-lived states. High solubility and the absence of bands belonging to the solvent in the area of interest is a prerequisite to perform experiments TRIR. When one is going to compare two different techniques, is desirable that the experimental conditions remain invariant. In the case of the measurements performed in ethanol, this requirement could not be respected, due to the presence of solvent bands in the spectral region of 1550- 1650 cm^{-1}, which constitutes the region of the ethylenic moiety vibrations for our molecule. Therefore, the TRIR experiments were performed on chloroform solution, whose absorption bands fall at lower frequencies, in a region not interfering with vibrational bands of the sample.

Parameter	Ground State S_0	Excited State S_1
C_1-C_2 [a]	1.49	1.48
C_4-C_5 [a]	1.46	1.42
C_5-C_6 [a]	1.36	1.39
C_6-C_7 [a]	1.45	1.43
N_1-C_1-C_2 [b]	117.3	120.6
C_1-C_2-N_2 [b]	117.3	115.1
C_3-C_4-C_5 [b]	124.5	126.0
C_4-C_5-C_6 [b]	126.7	127.7
C_5-C_6-C_7 [b]	125.7	124.8
C_6-C_7-C_8 [b]	131.0	131.5

Table 3.2: Selection of the geometric parameters optimized for the ground state (S_0) and for the first excited state (S_1).[(a)] are the bond length in Å; [(b)] are the angles.

Transient spectra obtained for 2DA in chloroform solution are shown in Figure 3.7. The most prominent features in these spectra are negative ground-state bleaching bands centered at 1589 and 1625 cm^{-1}. The first bleach signal decays with two components, the shorter with a time constant of 38 ps and the longer one with a time constant of 600 ps. The other bleaching band is too weak for analyzing it without excessive error. There is also present a weak positive band centered at 1560 cm^{-1} with a FWHM of 34 cm^{-1}. This positive band is partially obscured by the nearby bleaching bands. This last band decays with two components, a shorter one with time constant of 5 ps and a longer one with time constant of 61 ps.

Direct comparison of the long delayed transient spectrum and the inverted ground-state absorption spectrum, showed in Figure 3.8 clearly indicates that the signal neat 1589 cm-1 is not a pure bleach, but it is affected by a positive band probably due to displacement at low frequency of the band in 1620 cm^{-1}, as has been confirmed by the calculated frequencies of the excited state.

Frequency (cm^{-1})	τ_1 (ps)	A	$\tau_2(ps)$	A
1555	5.3 ± 3	0.03	61 ± 10	0.04
1589	38 ± 0.9	-0.08	606± 40	-0.07

Table 3.3: Fit parameter for the magic angle kinetics in Chloroform.

The direct comparison of these results with those obtained using the

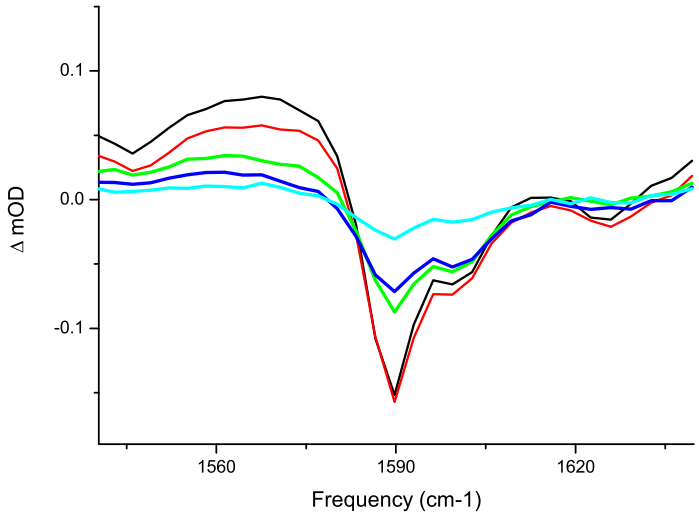

Figure 3.7: Transient Infrared Spectra following the excitation at 400 nm in chloroform from 1 ps (*black*) to 500 ps (*cian*)

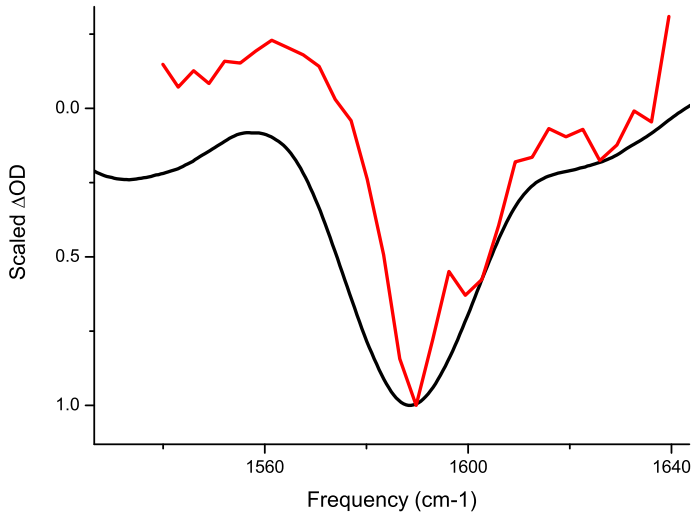

Figure 3.8: Normalized transient mid-IR spectra of 2DA in Chloroform at 500 ps after the excitation at 400 nm (*red*). The ground-state IR absorption of 2DA is also shown inverted and scaled for comparison (*black line*)

transient absorption technique is not possible because the experimental conditions are completely different, the use of different solvents changes the characteristics of the excited states and hence, the dynamics of photoinduced process. As in ethanol solution has not been possible to make measurements at TRIR, we measured in other alcohol, in methanol. The most remarkable

Frequency (cm^{-1})	τ_1 (ps)	A	$\tau_2(ps)$	A
1555	6.48 ±1.5	0.06	123 ± 16	0.06
1589	1.69 ± 0.4	-0.04	215± 20	0.43

Table 3.4: Fit parameter for the magic angle kinetics in Methanol.

feature of the measurements performed in methanol is the lower intensity of the positive band this could be a consequence of a lower frequency shift of the absorption band with respect to the measurements performed on chloroform. Possibly, that could be de cause of the apparent grow of the bleaching intensity, as we can see in the amplitude of preexponential A_1 that is negative , which means an increase in the intensity of the bleaching band, this is only possible if there are another positive bands below.

The agreement between the lifetime of the excited state found using the TA and found using time resolved IR spectroscopy is excellent, the differences may be due to the different characteristics of ethanol and methanol. Regarding the relaxation time to the ground state found in the bleaching in the transient spectrum in the infrared region, is significantly longer than that found in the electronic spectrum, such difference between the TRIR and TA data can be rationalized in terms of the formation of a vibrationally hot ground electronic state which would be silent in transient absorption measurements but would render a signal in the TRIR spectrum. Thus, the long component of 215 ps in the transient decay and parent recovery registered in the TRIR experiments is attributed to the lifetime of the vibrationally hot ground electronic state. The formation of vibrationally hot ground states has been documented when the ground-state is populated from an electronic excited state within several picoseconds, considerably faster than intermolecular cooling of either state can occur. The time scale of cooling of vibrationally hot ground states of large molecular systems has been reported to lie in the range from several picoseconds to several tens of picoseconds.[58,59]

3.6 Conclusions

From all the data collected, we can assume that the simplest reaction model is a pure sequential one, in which the reaction starts at I_1 (charge transfer

excited state) and continues to a hot excited state, and then relaxation to the ground state, as we can see in the Figure 3.9. Excitation of 2DA by UV/Vis light populates the Frank Condon region (FC^*, I_1) in a vertical transition. It is well known that optical excitation generates the excited electronic state with a huge amount of vibrational energy excess. In addition, displacement of electron density can occur which leads to (partial) inversion of single- and double-bond characters. The excess of vibrational energy leads to fast initial configuration changes, and intramolecular vibrational energy relaxation. The molecular state populated in this reaction can be described as a relaxed stated (I_2).

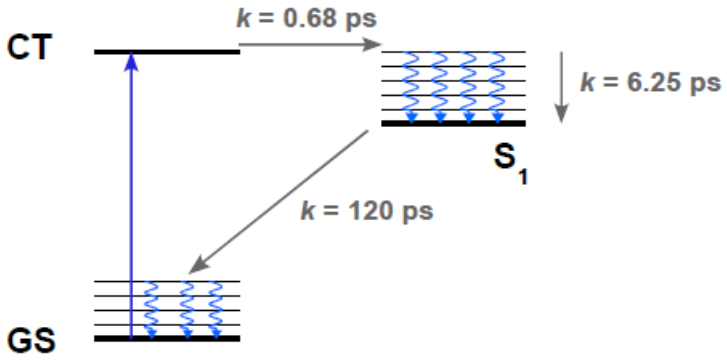

Figure 3.9: Scheme of energy levels

4

Acceptor-Donor-Acceptor [4DA]

4.1 Absorption and Emission Spectra

The absorption and fluorescence spectra of diluted solutions (c = 5 10^{-6} M or less) in ethanol are reported in figure (4.1) and (4.2) . The dye shows an intense intramolecular charge transfer with two maxima at 436 and 445 nm. Three Gaussian lines were necessary in order to describe the experimental spectra, centered at 410, 434 and 456 nm, with relatively intensities of 1.96, 1 and 0.3, respectively. The agreement between the calculated TDDFT absorption spectra and experimental absorption maxima is excellent (450 vs 436 nm). The analysis of the TDDTF eigenvectors allows us to assign the nature of the excited states responsible for the absorption spectra. The lowest transition, corresponding to the HOMO→ LUMO excitation is symmetry forbidden, and does not contribute to the absorption spectra. This dark excited state is followed by an, almost two degenerated, transition involving the HOMO-1→ LUMO centered at 426 nm (f=0.6), and the transition the HOMO→ LUMO+1 centred at 457 nm, that dominates the absorption spectra due to it strong intensity (f= 3.3).[55] The molar extinction coefficient value is in the order of 130 000 mol^{-1} L cm^{-1}.

The emission spectra of the dye, see figure (4.2), show clearly two maxima at 491 nm and 512 nm. Three Gaussian lines were necessary to describe the experimental emission spectra, but it is situation where contributions of individual states remained unresolved, appearing as a pattern of broad bands. The lines of Gaussian fit are centered at 543, 508 and 481 nm, and the ratio of intensities is 0.66, 1 and 0.4 respectively. The adiabatic transition calculated by TDDFT ΔE is 2.47 eV (502 nm) in in perfect agreement with

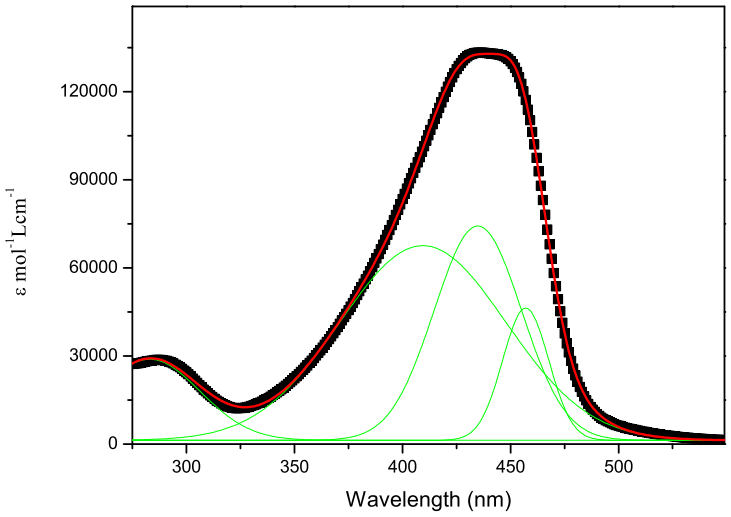

Figure 4.1: UV-Visible spectra (*blackline*) solvent EtOH plotted together with a Gaussian fit (*red*) and individual Gaussians are shows in *green*.

experimental data.

The absorption and emission properties of the dye can be compared with the building units, in order to evaluate the effects of the linkage of two donor-acceptor heteroaromatic arms through a bipyridine core.[60] As expected, a bathochromic effect is present upon linking the "monomers" in the bipyridine "dimers", as a consequence of the elongated π-frameworks. The "monomer" shows a maximum of absorption at 415 nm and a maximum of emission at 490 nm in methanol; for the "dimer" the maxima are at 436 nm and 491 nm respectively. The photophysical parameters (absorption and emission) in several solvents are collected in the Table 4.1.

Table 4.1: tabla blala

solvent	$\lambda_{abs}[nm]$	$\lambda_{em}[nm]$	Φ_F
EtOH	441	491	-
MeOH	445	501	-
MeOH-d4	445	496	-
DMSO	448	501	0.016

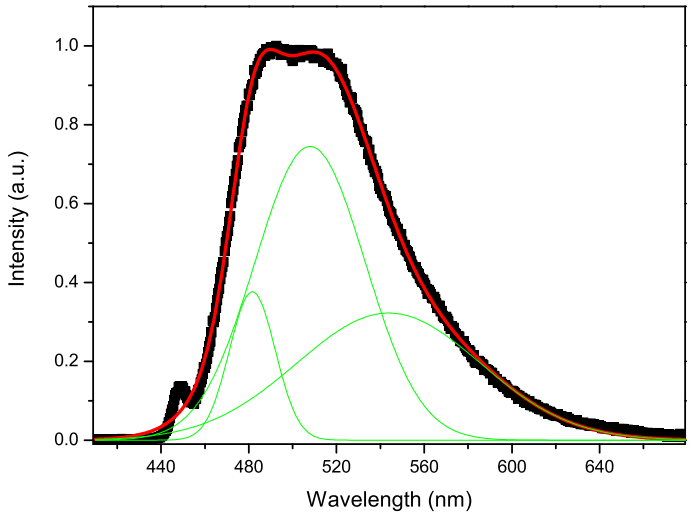

Figure 4.2: Fluorescence spectra (black line) solvent EtOH plotted together with a Gaussian fit (red) and individual Gaussians are shows in green.

4.2 Fluorescence lifetimes

The samples are excited by tunable femtosecond pulses obtained from the laser apparatus described for TAS. The fluorescence is collected by a quartz lens and focussed onto the photocathode of a Hamamatsu R2809U-01 microchannel plate photomultiplier, after elimination of the excitation beam scattered radiation, by means of an appropriate set of colored filters. The photomultiplier signal is fed into a digital oscilloscope (2.5 GHz band-pass). The slightly asymmetric instrumental function, measured by light scattering from a latex solution, has a time duration (FWHM) of 550 ps, highly reproducible from one experiment to another. The experimental time profiles were deconvoluted taking into account the instrumental function, and were fitted by exponential functions, obtaining intrinsic fluorescence lifetimes. The excitation wavelength is 400 nm, in resonance with the intramolecular charge transfer (for the details of the instrumental apparatus, see the Chapter 2.2).

The solutions were freshly prepared using methanol, deuterated methanol and ethanol as solvents We have prepared the solutions using the technique described in Section 2.4.

The fluorescence time profiles of the solutions have been measured and

are shown in Figure (4.3).

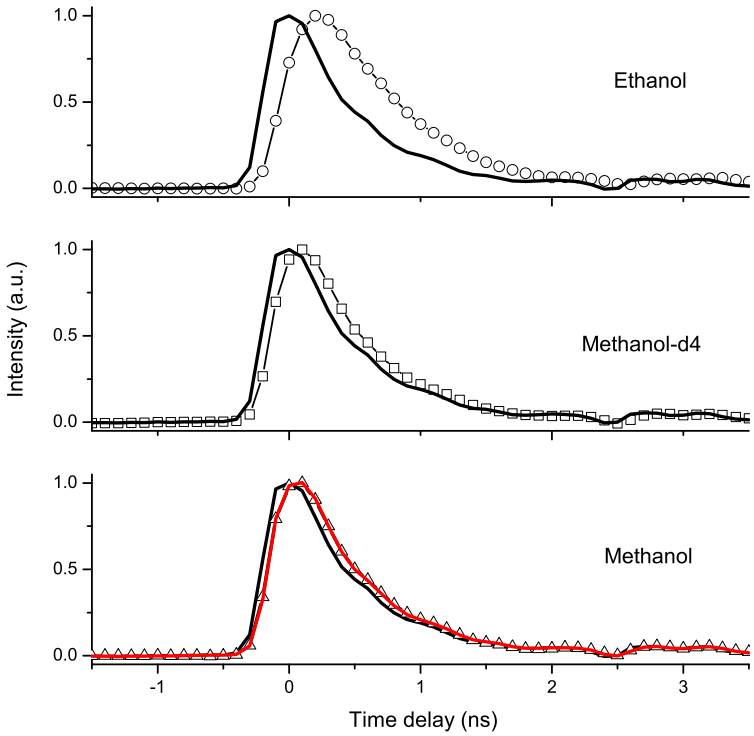

Figure 4.3: The time profiles of solutions in ethanol (*upper panel*), methanol-d4 (*middle panel*),and methanol (*bottom panel*). The instrumental function (*full black line*) is also shown in the figure. The results of decovolution/fitting procedure with a single exponential function is shown with a *solid red line*

The fluorescence evolves in a time interval comparable to that of the instrumental function. The lifetime is shorter than 550 ps, but cannot be determined with accuracy applying the deconvolution procedure. Even so, all the time profiles fluorescence are monoexponetial, being hte time constant in ethanol 0.3 ns, while the time constant calculated for the solution in methanol-d4 is =0.089 ns, whereas for the solution in methanol was found to be faster: 0.055 ns, in good agreement with the TAS experiments.

4.3 Transient Absorption Spectroscopy

In order to properly apply the fitting procedure we have to correct the temporal shift between the various kinetics, introduced by the group veloc-

ity dispersion (GVD). The instrumental function (cross-correlation between pump and probe pulses) was measured as described in section X; the fitting procedure yields a gaussian shape function with 200 fs FWHM. The "zero time" is obtained by an initial measurement session of transient spectra in which the delay associated to the maximum of the SRG is identified. Thus, we obtain the absolute delay value at which we have temporal coincidence between the pump and the portion of the probe pulse whose wavelength corresponds to the maximum of the SRG.

4.3.1 Measurement in Ethanol

In the Figure (4.4) we report the transient absorption spectra of 4AB in ethanol, in the spectral range 420-650 nm. The TA spectra in the picture was recorded at several delay time with respect to the photoexcitation at 400 nm in resonance with the intramolecular charge transfer transition. They show two negative bands around 450 and 550 nm, corresponding to the bleaching of the ground state and to the stimulated emission respectively; one positive band at 520 nm, and another one between 600 and 650 nm, corresponding to the excited state absorption are observed. The signal at ~ 457 nm, that disappears within 200 fs and is due to the SRG of the solvent.

In order to properly apply the fitting procedure we have to correct the temporal shift between the various kinetics, introduced by the group velocity dispersion (GVD). The instrumental function (cross-correlation between pump and probe pulses) was measured as described in section X; the fitting procedure yields a gaussian shape function with 200 fs FWHM. In single wavelength experiments, the "zero time" is obtained by an initial measurement session of transient spectra in which the delay associated to the maximum of the SRG is identified. Thus we obtain the absolute delay value at which we have temporal coincidence between the pump and the portion of the probe pulse whose wavelength corresponds to the maximum of the SRG.

A very broad ESA band appears simultaneously with the excitation (within the instrument function). This signal is distorted due to the overlap with the SE band. In the first picoseconds after the excitation, the ESA band shows a blue shift of the maxima, while at same time the intensity of SE band centered at 550 nm increases and undergoes a blue shift. In order to fully characterize the spectral dynamics, we have measured the kinetics profiles at 436 nm, 510 nm and 550 nm, in correspondence with B, ESA, and SE, respectively. Three time constants were necessary for a satisfactory fitting of the bleaching band (B), using

(4.1)

with time constants $\tau_1 = 1,2$ ps , $\tau_2 = 21,6ps,$ ps which contribute to the

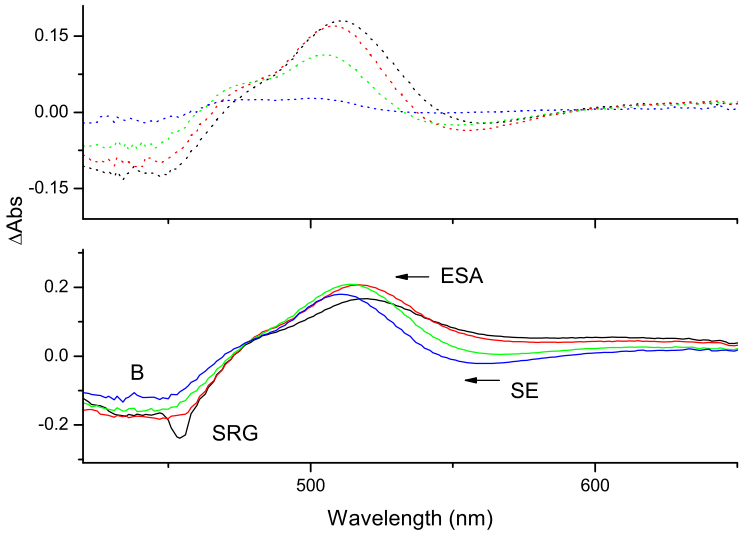

Figure 4.4: Transient absorption spectra of dye in ethanol exciting at 400 nm, at selected delay times.The ESA, SRG, B and SE symbols identify transient bands due to excited-state absorption, stimulated Raman gain of the solvent, bleaching and simulated emission, respectively.In the lower panel, the transient spectra in the first 5 ps are shown: temporal coincidence between pump and probe pulses (black solid line), at 200 fs(red solid line), 1 ps (green solid line) and 5 ps (blue solid line). In the upper panel, the evolution of the transient spectra is displayed after 5 ps: 5 ps (black dotted line), at 20 ps (red dotted line), 100 ps (green dotted line) and 500 ps (blue dotted line). The arrows indicate the time changes of the signals.

relaxation from the excited state to the ground state. The experimental features with three picoseconds time constant suggest that the reaction model that must be considered should be one in which three intermediates exist in addition to the ground state. As we can see in the Figure 4.5 all the preexponential time constants are negative, indicating a decrease the signal intensity.

For a satisfactory fit of the ESA band, only two components are necessary, with time constants $\tau_1 = 13$ $\tau_2 = 303$ ps. The second component has a positive amplitude, whereas is negative for B, indicating that this time constant corresponds to the decay time at 500 nm and to the rise time at 435 nm of the same relaxation process.

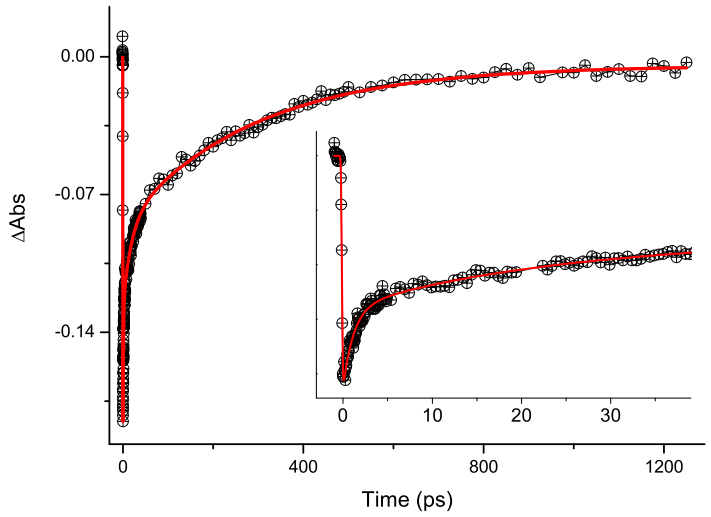

Figure 4.5: Kinetics profile (open circles) recorder at 435 nm in correspondence with the center of the bleach band . The inset panel show the transient absorbances at the probe wavelengths for short delay times.

4.3.2 Measurements in Methanol

The transient absorption spectra were measured using methanol as a solvent. In this case the white continuum was generate with a sapphire wedge and the spectral range covers 450-900 nm whereas for CaF_2 the spectral range covers 350-750 nm. For this reason, we can not see the bleaching band under 450 nm, which probably was partially overlapped with the ESA band. A very broad ESA band appears at 490 nm, simultaneously with the excitation (within the instrument function). Partial overlap between the ESA and the SE was observed. Due to the weakness of the SE band in the first 150 fs, is difficult to observe if it appears instantaneously, or with some delay. As we see in the figure (4.6) the signal at 540 nm is negative only after 200 fs.

In order to fully characterize the spectral dynamics, we measured the kinetics profiles at 490 nm and at 540 nm. Representative results along with multi-exponential fits are reported in Fig (4.7). For the ESA two time constants were necessary for a satisfactory fit of the experimental data, for the ESA band the fit was done following equation (4.2), where the first time components were obtain from the fit of ESA and remained constant. The fitting procedure was done in this way because the proximity of the ESA

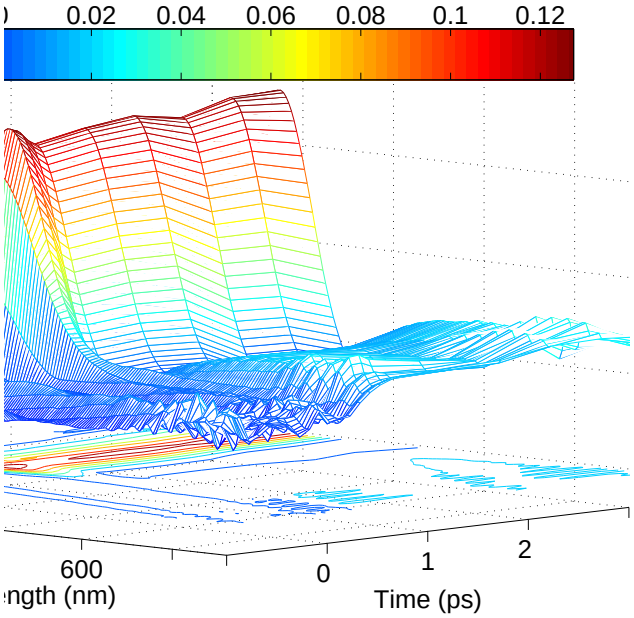

Figure 4.6: Tri-dimensional plot of ΔA as a function of the delay time and the wavelength. The spectral distortion due to GVD have been corrected and the data are collected in matrix A(λ, t).

disturbed the dynamics of SE.

$$R(t,\lambda) = P_{ESA}\Big(\sum_i A_i(\lambda) exp(-t \setminus \tau)\Big) + P_{SE}\Big(\sum_i A_i(\lambda) exp(-t \setminus \tau)\Big) \qquad (4.2)$$

The corresponding time constants obtained from the deconvolution/fitting procedure are $\tau_1 = 74{,}39$, $\tau_2 = 1.13$, $\tau_3 = 1.13$, $\tau_4 = 35.3$ In the first 20 ps a blueshift of the maxima of both SE and ESA bands is observed, with a value of 9 nm.

4.3.3 Measurements in Methanol-d4

In order to characterize the spectral dynamics due to the different solvents, we realized the same experiment using tetra-deuterated as a solvent methanol (MeOH-d4). The position of the maxima of the ESA and SE bands is the same that in the transient absorption measurements performed on methanol solutions, however the dynamics of these bands presented small differences, as we can see in the figure (4.8) (the signal is normalized for a best comparison). One ps after the excitation at 400 nm, (upper panel) the ESA in methanol-d4 is narrower than in methanol, but the relative intensi-

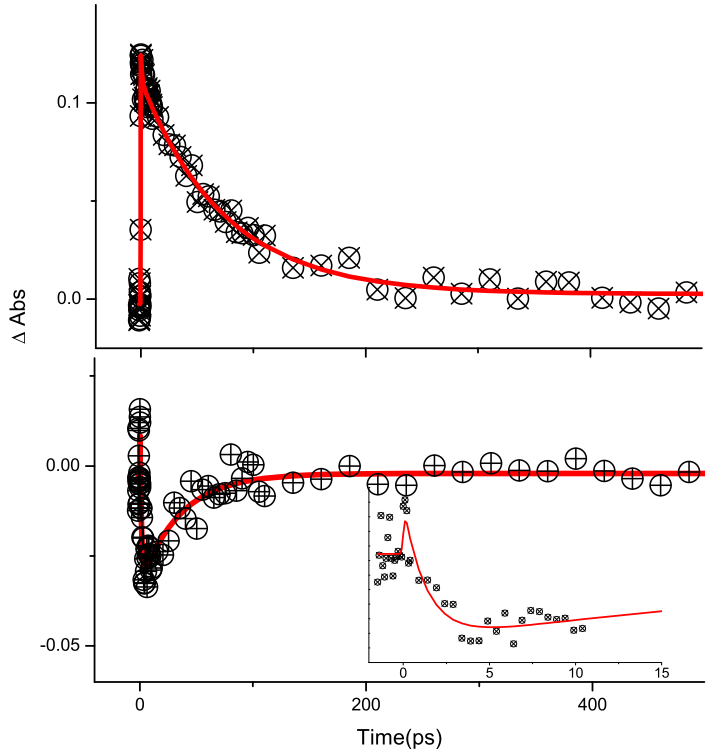

Figure 4.7: Kinetics profiles (*open circles*) recorded at 490 nm (*upper*)and at 540 nm (*botton*) for the compound in methanol. The inset of the panel shows the behavior for short delay times.

ties are the same for ESA and SE bands in both solvents. 30 ps after the excitation the relative intensity of SE in normal methanol is smaller, and the ESA band is broader than in methanol-d4.

The dynamics of the ESA band can be described with a bi exponential function with time constants $\tau_1 = 3.9 \pm 0.3$ and $\tau_2 = 89.8 \pm 5$ ps. The amplitudes of the time constant are negative for the two components, indicating a decrease in the intensity of the band. The first time component coincide with the time constant found for the apparent blue shift of the band. The amplitude for this first time constant (A_1) is smaller than the 10% of the amplitude for the second time constant A_2, being the ground state decay the principal process.

The SE band was fitted with the equation (4.2), obtaining the time constants $\tau_3 = 320 \pm 50$ fs and $\tau_4 = 86.2 \pm 4$ ps. τ_1 and τ_2 correspond to the time constants found in the ESA fitting, and were considered as constants in this deconvolution/fitting procedure. The shortest time τ_3 has a negative

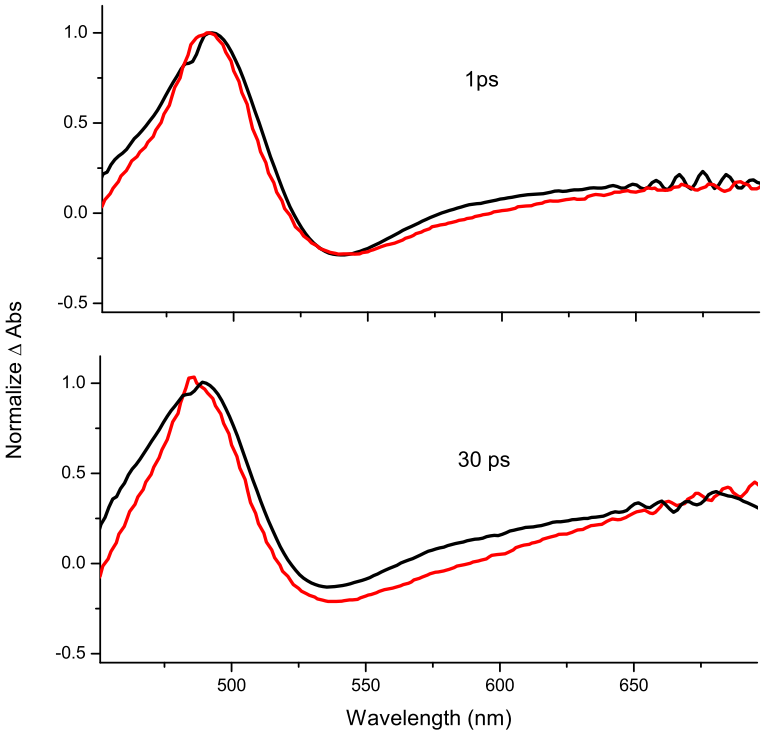

Figure 4.8: The *upper* panel shows the transient absorption spectra 1 ps after the excitation at 400 nm. The solution in deuterated methanol (red) and normal methanol (black). The *bottom* panel shows the transient absorption spectra 30 ps after the excitation

amplitude (increase the intensity) while the longest time τ_4 has a positive amplitude, indicating that this is the time constant of the decay to the ground state.

4.3.4 Single Value Decomposition

Once applied the GVD correction, we performed a decomposition of the family of spectra taken at different delay times, with the help of the singular value decomposition (SVD) method (SEction X). The standard SVD algorithm, which uses the LAPACK routines to computes matrix decomposition, was implemented in a home-made program. SVD, combined with a subsequent target analysis, is a powerful procedure which allowed us to extrapolate the spectra and the temporal evolution of the vibrational and electronic (decay of excited state population) relaxations. We performed

Table 4.2: Multiexponential fittings of the observed kinetic profiles shown in Figs (4.5), (4.7), time constants (τ, ps), amplitudes (A) and wavelengths (λ, nm). Decay processes correspond to positive amplitudes while rise processes to negative amplitudes.

EtOH			MeOH			MeOH-d4		
λ_{probe}	A	τ	λ_{probe}	A	τ	λ_{probe}	A	τ
	0.07	1.2 ± 0.1						
430	0.04	21.6 ± 2.7						
	0.08	328.9 ± 15						
499	0.007	13.4 ± 3.7	496	0.01	1.01 ± 0.3	496	0.004	3.9 ± 0.3
	-0.15	304± 9		0.11	74.4 ± 3		0.065	89.76± 3
551	-0.08	0.57 ± 0.05	540	0.047	1.3 ± 0.3	540	-0.017	0.32 ± 0.03
	-0.07	6.54 ± 3.7		-0.031	35.35 ± 4		0.10	86.19 ± 3
	0.045	208.34 ± 9						

the SVD analysis on the matrix associated to the spectra at the magic angle condition, according to the relation:

$$A(\lambda,\tau)_{ma} = UST^T \qquad (4.3)$$

As we have seen in the previous section, SVD decomposes the original data into three matrices (U, S, V), reducing the whole set of spectra to a limited number of orthogonal basis components. The number of the significative basis spectra is determined by the weight of the elements in the matrix S.

The SVD analysis was performed for all data, here we will comment the SVD analysis for the measurements performed in ethanol.

The decomposition procedure gave three main components characterized by singular values $S_{11} = 11.7$ and $S_{22} = 2.7$ and $S_{33} = 1.3$. In Figure (4.4) we display the spectra corresponding to the three major SVD components, scaled according to the respective singular values. As an indicative general rule, our experience suggests to consider only the components whose singular values are greater than 10 % of the first element S_{11}. So, the non-negligible N columns (in this case, N = 3) of the V matrix are multiplied by their respective singular values (SV), and simultaneously fit to a sum of M

exponentials.

$$SV_N(t) = \sum_{m=1}^{M} C_{nm} \cdot e^{-t/\tau} \tag{4.4}$$

The resulting kinetic profiles are shown in Figure (4.10). M is the minimum number of time constants necessary to globally fit all the N SVD component. The parameters are shown in Table 4.3.

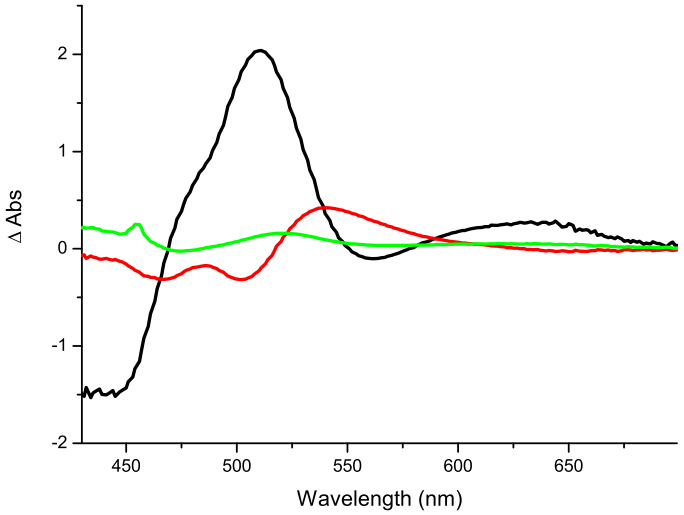

Figure 4.9: Basis spectra U_1 (black), U_2 (red), and U_3 (green) . The ΔAbs values are scaled according to the single value S_N .

Due to the presence of a strong cross-phase modulation (XPM)[61] artifact during the first hundreds of femtoseconds, we will not discuss the evolution within this time interval. The instrumental function was determined following the procedure described previously, obtaining a gaussian-shape function with ~ 200 fs FWHM. We simulated the coherent effect (XPM) by the convolution of the instrumental function with a δ-type function. Instead, the evolution of V_1, V_2 and V_3 was simulated by the convolution of the instrumental function with a three-exponential kinetic model. The parameters of the model function were simultaneously optimized on V1 and V2 kinetic traces by means of a home-developed global fitting programm.

The spectral basis and the correspondent time course vectors have not a physical meaning, but for each decay it is possible to construct the associated spectra (DADS) by the following equation

$$(DADS)_m(\lambda) = \sum_{n=1}^{N} C_{nm} \cdot U_n(\lambda) \tag{4.5}$$

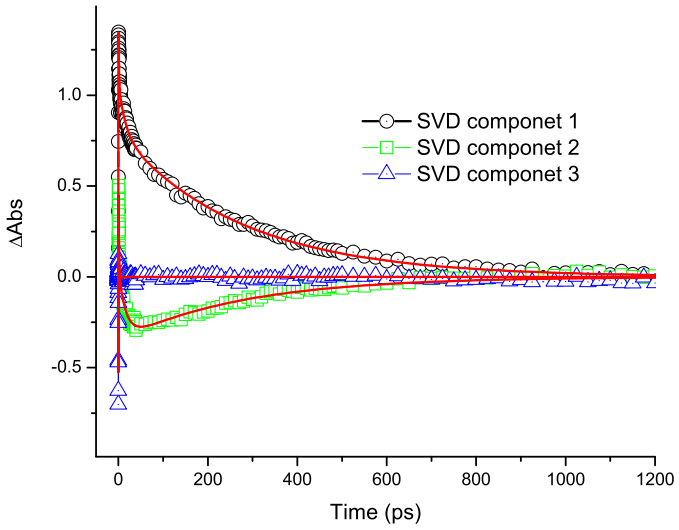

Figure 4.10: Time courses of SVD componets of ethanol data and fitting curves (red). The ΔAbs values are scaled according to the single value S_N.

	1.3 ±0.1 (ps)	16.1 ±0.4(ps)	276 ±10(ps)
SV_1	0.339	0.494	0.142
SV_2	0.266	0.386	-0.008
SV_3	0.790	-0.353	0

Table 4.3: Parameters for a simultaneous fit of time courses of single value decomposition components, with a three exponential model.

the spectrum associated to each one of the m exponential components is obtained from a set of N coefficients C_{nm}. The three DADS obtained with this method are shown in the Figure 4.11.

4.3.5 Fluorescence Maximum Shift

If we look at TAS spectra Fig(4.4) and Fig(4.6), we can see that a shift of the maximum of the SE band occurs in the first picoseconds. Whether this latter is due to an intramolecular dynamics or is due to solvent rearrangement can be understood after the construction of the corresponding correlation function and its comparison to previous data.[62,63] The dynamics Stokes

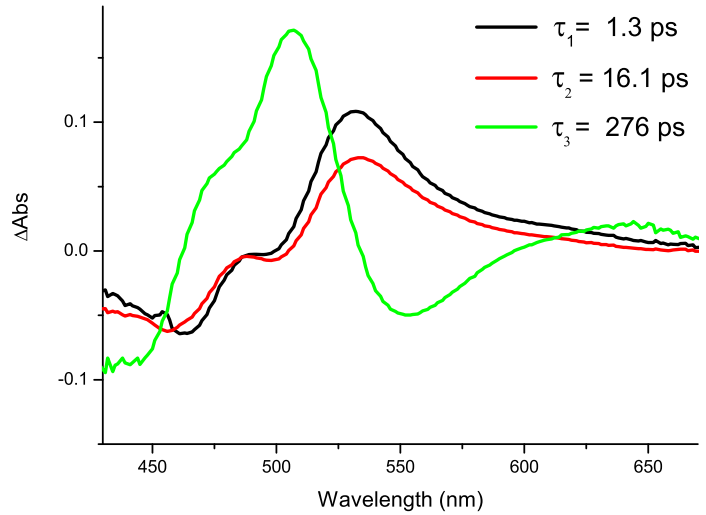

Figure 4.11: Spectral components of the three time contributions to the transient absorption signal in ethanol. $DADS_1$ in black, $DADS_2$ in red and $DADS_3$ in green.

shift function is defined, as we said previously, as

$$S(t) = \frac{\overline{\nu}(t) - \overline{\nu}(\infty)}{\overline{\nu}(0) - \overline{\nu}(\infty)} \tag{4.6}$$

In our experiments we used the SE to derive the Eq. 4.6,.[?] As a matter of fact, contrary to the fluorescence spectra obtained by up conversion or directly registered by streak cameras, the shape of SE is distorted, showing that stimulated effects can modify the band and change its maximum position. This expression is used often when the shift occurs from hight energy states to low energy ones, in other words the shift that we see is a red shift, i.e. $\nu(0)$ is greater than $\nu(\infty)$.

As we can observe in the upper panel of the Figure 4.17, this is not the case described before; at time $\tau(0)$ the maxima of SE band is at 17600 cm^{-1} while $\nu\infty)$ is 18350 cm^{-1}, appearing like a blue shift. The blue shifts of the emission bands are usually attributed to phenomena like excite-state reactions, proton transfer,[64] and intramolecular rearrangements or isomerization,[65].[66]

The direct comparison of the stimulated emission and the spontaneous emission is not possible because the stimulated emission is disturbed by an intense excited-state absorption band. But is clear the presence of a phe-

nomena that seems a dynamic blue shift of the SE band. In order to explain this process we can consider the possibility of the existence of two different excited states. The dual luminescence, associated with the existence of two different singlet excited states, has been observed in polar solvents. The intramolecular charge transfer in the excited state takes places in a variety of other molecules like aminobenzonitriles, donor/acceptor stilbenes substituted, biantryls, etc. In this molecules dual emission from a locally excited state (LE) and a charge transfer state is already observed in the spontaneous fluorescence spectra.[67,68]

If we observe the spontaneous emission spectra (Figure 4.2) is clear that we have at least two different states, one peak at 18400 cm^{-1} and another one at 20750 cm^{-1}, the separation is ~ 2000 cm^{-1}, whereas the separation between the SE maxima is ~ 700 cm^{-1}.

If we compare the emission spectra of this molecule with the one of the simplest bipyridine-π-donor molecule, we observe a red shift that can be attributed, among other factors, at the presence of the second acceptor, the terminal-pyridine moiety. Is probably that the intensity of stimulated emission from the external moiety will decay faster than the stimulated emission from the bipyridine moiety, resulting is an apparent blue shift of the total band. As we can see from the magnitude of the shift and the dynamics, depends of the solvent.

The results of the shift analysis in three different solvents provided the correlation curve reported in the Figure (4.17). The corresponding time constants of the shifts, obtained by a fitting procedure with a single exponential function are 21 ± 0.5 for ethanol, 3.7 ± 0.2 for methanol and 3.9± 0.2 for methanol-d4 .

In ethanol (Figure 4.17, panel A), the maximum of the SE band shifts from 17.600 cm^{-1} to 18.310 cm^{-1} between 0 and 100 ps, whereas in methanol and deuterated methanol, the shift is smaller, ranging from 18.250 cm^{-1} to 18.650 cm^{-1} between 0 and 20 ps .

4.4 Steady state FTIR Spectra

The steady-state FT-IR spectra were recorded (see Figure **??**)in chloroform, methanol-d4, and methanol as solvents. The solutions were prepared in dry box under N_2 atmosphere. The solutions were held between CaF_2 windows separated by a 100 μm thickness teflon spacer.

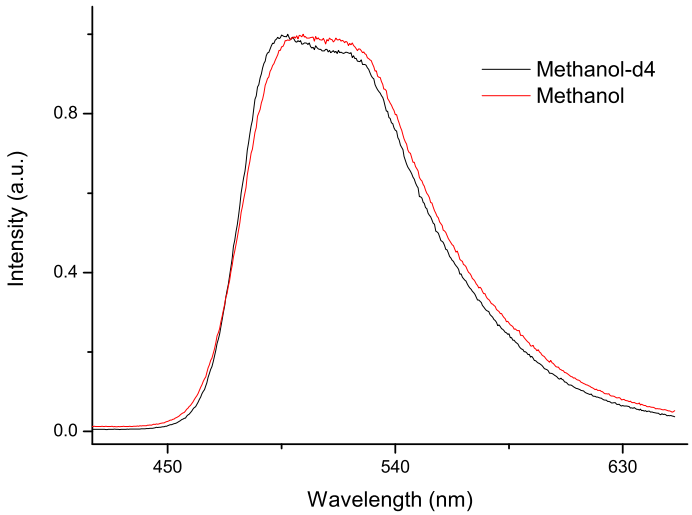

Figure 4.12: fluorescence methanol methanol-d4

4.5 Time-Resolved Infrared Spectroscopy (TRIR)

Femtosecond TRIR experiments were conducted at probe frequencies between 1530 and 1640 cm^{-1}, in order to observe the short-time dynamics of the 1585 cm^{-1} and 1620 cm^{-1} was performed in methanol-d4, methanol and chloroform. In ethanol the measurements didn't could be performed because the FTIR bands of the compound was covered for the ethanol bands, and the probe pulse was too weak.

4.5.1 Measurement in Chloroform

Transient infrared spectra of chloroform solution of the dye have been recorded, after 400 nm excitation, for delays from -2 to 1400 ps. The pump probe signal measured for parallel and perpendicular polarization of pump and probe are use to calculate the magic angle signal(MAS) in order to eliminate the orientational contribution to the kinetics:

$$MAS = \frac{I_{\parallel} + 2I_{\perp}}{3} \tag{4.7}$$

Representative transient infrared spectra at various delay time are shown in Figure 4.18. The measurements was recorded in the region from 1530 cm^{-1}. and 1640 cm^{-1}, here the FTIR shown a broad band peak at 1587

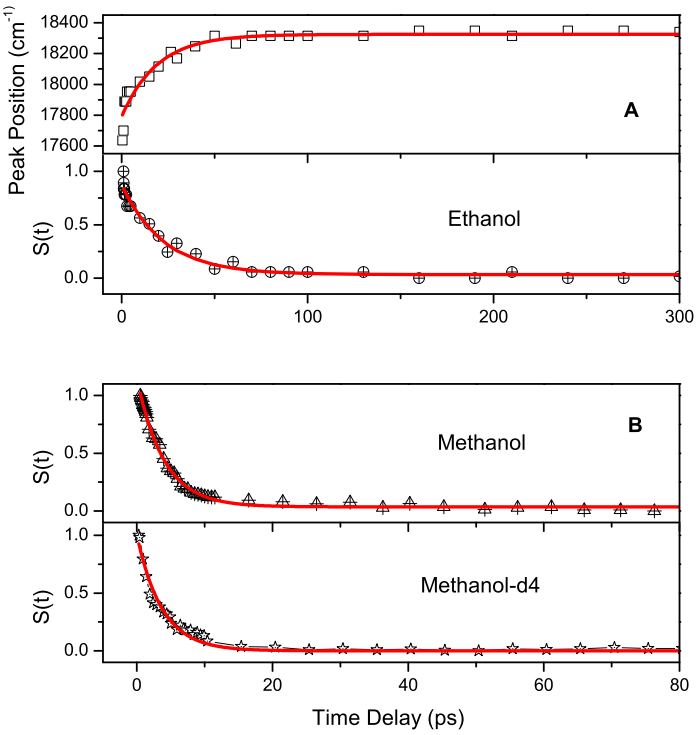

Figure 4.13: (A) (*Upper panel*) Peak position of the SE band against time delay. (*Bottom*) The kinetic traces of the dynamical Stokes shift (*open circles*) using as solvent ethanol. The results of the fitting analysis whit a single exponential function (time constant: 21±0.5) is shown in red solid line. (B) (*Upper panel*) The kinetic traces of the dynamical Stokes shift (*open triangles*) using as solvent methanol, the best fit with a single exponential decay is shown in *red solid* line (time constant: 3.7±0.2). (*Bottom panel*) The kinetic traces of the dynamical Stokes shift (*open stars*) using as solvent deutered methanol the best fit with a single exponential decay is shown in *red solid* line (time constant: 3.9±0.2)

cm^{-1} with a shoulder on the high energy side at 1595 cm^{-1}., and a weak band at 1619.6 cm^{-1}.

In the time resolved infrared data we observe a very intense broad positive band centered at 1554 cm^{-1}, a weak bleaching band at 1585 cm^{-1} and 1592 cm^{-1}, and make out a bleach at 1619 cm^{-1} too weak for an analysis of the dynamic. Transient difference spectra shows an instantaneous build-up of bleaching bands and transient absorption bands. Transient kinetic decays are shown in Figure Kinetics. Negative signals occurring just before time

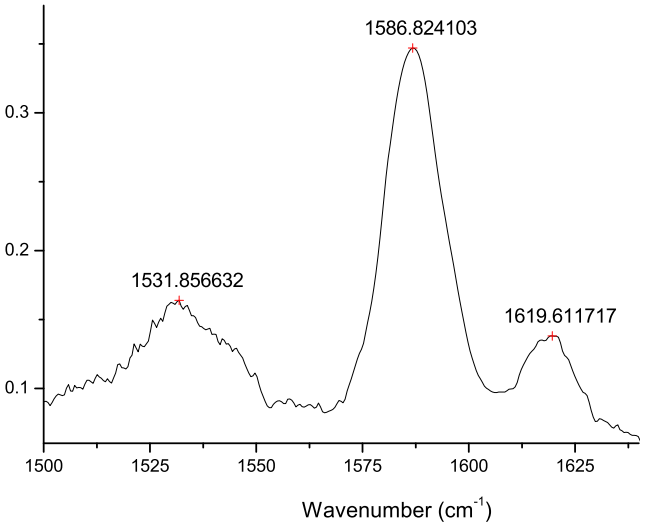

Figure 4.14: FTIR CHCl3

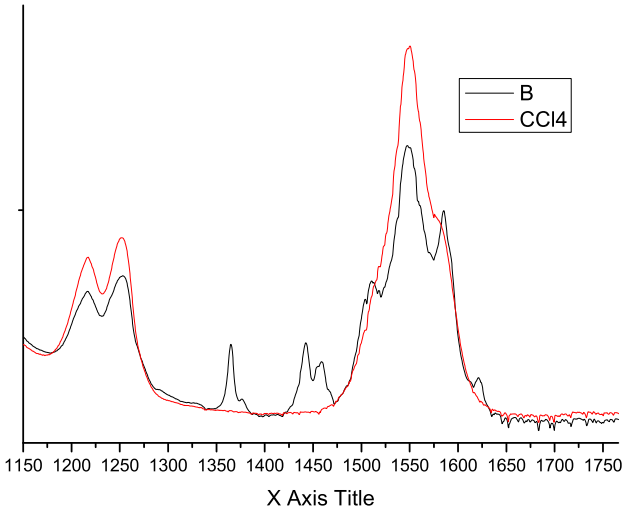

Figure 4.15: FTIR CCl4

zero are due to perturbed free-induction decay.[69] A strong but short-lived spike occurs around zero time delay at all probe frequencies due to cross phase modulation (XPM). For this reason the fitting process was realized

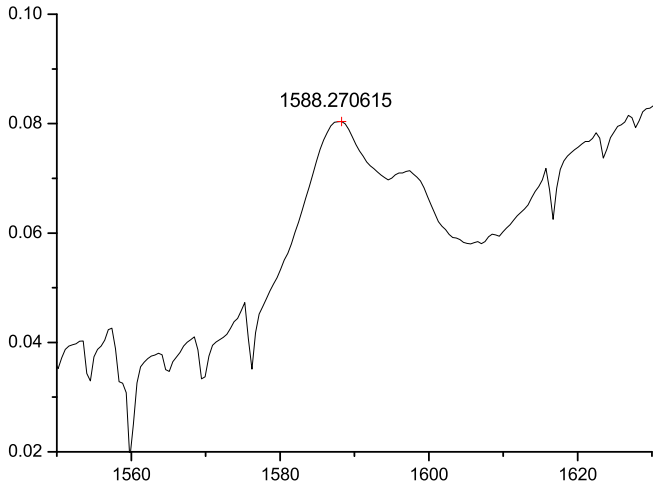

Figure 4.16: FTIR MeOD

after the first picosecond. The results of fitting process shows in the Table **??**.

Frequency (cm^{-1})	τ_1 (ps)	A	$\tau_2(ps)$	A
1554	18.9 ±3	0.03	235 ±20	0.07
1585	1.8 ±0.9	-0.018	235	0.023

Table 4.4: Fit parameter for the magic angle kinetics in Chloroform.

4.5.2 Measurement in Methanol-d4

Transient infrared spectra of methanol-d4 solution of the dye have been recorded, after 400 nm excitation, for delays from -2 to 1400 ps. The pump probe signal measured for parallel and perpendicular polarization of pump and probe are use to calculate the MAS.

The measurements was recorded in the region from 1530 cm^{-1} and 1640 cm^{-1}, here the FTIR shown a band peak at 1587 cm^{-1} and another band at 1597 cm^{-1}. In contrast to the FTIR registered in chloroform here the too bands are clearly distinguishable. The band at 1619 cm^{-1} is cover to the solvent band.

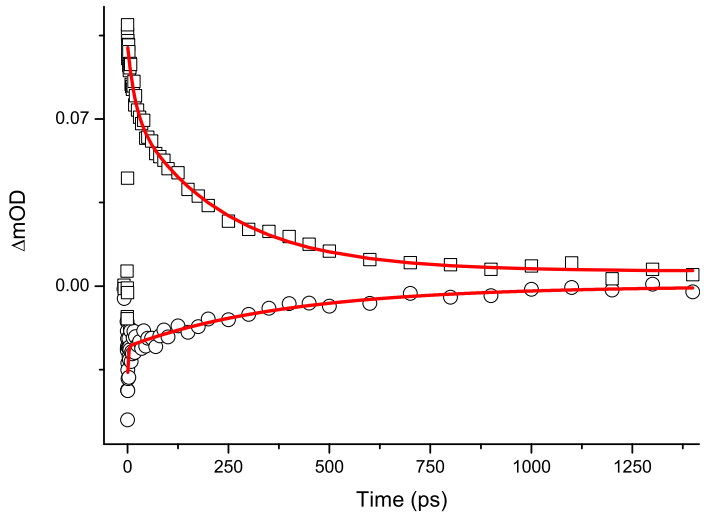

Figure 4.17: Transient kinetics of bypiridine following excitation with a femtosecond pump pulse at 400 nm in chloroform at 1554 cm^{-1} (*open squares*) and 1585 cm^{-1} (*open circles*)

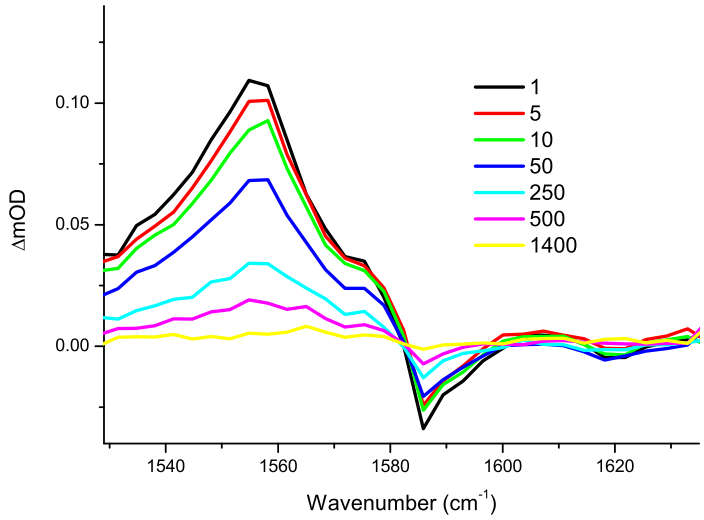

Figure 4.18: Transient Infrared Spectra following the excitation at 400 nm in chloroform from 1 ps (*black*) to 1400 ps (*yellow*)

In the time resolved infrared data we observe a very intense broad positive band centered at 1567 cm^{-1}, a weak bleaching band at 1587.8 cm^{-1} and 1596.5 cm^{-1}, and another weak bleach at 1617 cm^{-1}.

Frequency (cm^{-1})	τ_1 (ps)	A	$\tau_2(ps)$	A
1567	2.3 ±0.4	0.03	118.6 ±5	0.11
1587			157.6 ±20	-0.0361
1596			113.3 ±8	-0.04
1617			129.5 ±20	-0.02

Table 4.5: Fit parameter for the magic angle kinetics in Methanol-d4.

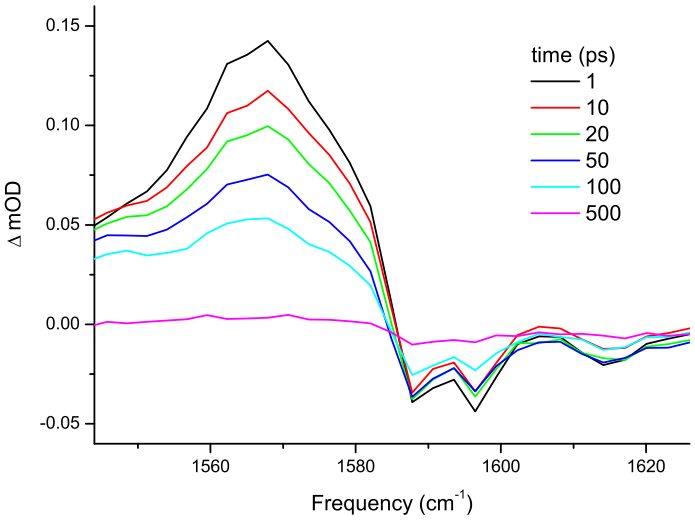

Figure 4.19: Transient Infrared Spectra following the excitation at 400 nm in Methanol-d4 from 1 ps (*black*) to 500 ps (*pink*)

4.5.3 Measurement in Methanol

For the measurements in MeOH the signal not decay in the range time of our experiment, the time constants for the bleaching are 21 ps and a long time constant of 3700 ps. If we fixed the long time constant like a constant we we can fit the data with a biexponetial function, in the Table **??** the fit parameters are reported. The measurements are very noisy, and show

only broad bleach and a very broad positive band. It is no possible see any signals in the FTIR in MeOH, there are hidden to the absorption band of the solvent.

Frequency (cm^{-1})	τ_1 (ps)	A	$\tau_2(ps)$	A
1560	2.7 ±0.6	1.2	107.2±15	0.82
1587			292.2 ±120	-0.036

Table 4.6: Fit parameter for the magic angle kinetics in methanol.

5

Acceptor-Donor-Acceptor Ion [4DA+]

The following chapter reports the measurements on the compound $4DA+$. This compound is structurally identical to the compound studied in the previous chapter, changing only the terminal pyridines by a methyl-pyridinium , that is now our molecule is positively charged. As we used the iodide counterion. The synthesis of this compound can be found in Abboto et al.[55]

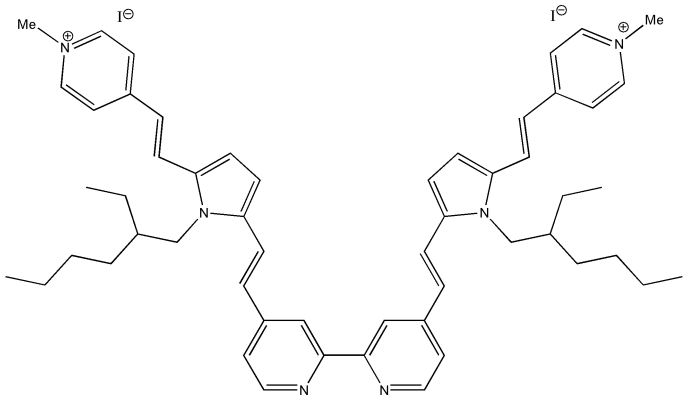

Figure 5.1: The molecule 4DA+.

As we have done for other compounds, we can compare the photophysical properties of this 'dimer' with the 'monomer' analog. The 'monomer' has an absorption band centered at 506 nm in methanol whereas in water the maximum is found at 480 nm. The dimer absorption band is centered at 515 nm in ethanol.[60] The monomer emission band is at 587 nm while the dimer

is centered at 590 nm. As expected, a small bathochromic effect is present upon linking the 'monomer' in the bipyridine 'dimers' as a consequence of the elongated π-framework.

We compare the neutral compound 4DA with the salt 4DA+ and found that the band of charge transfer is clearly red-shifted, from 441 to 516 nm using as a solvent ethanol. The iodide 4DA+ exhibit a strong single CT band in agreement with delocalization of the entire chromophore π system. The CT features associated with positively charged fragments are bathochromically shifted ($\Delta\lambda_n^+$) compared with the neutral precursor, due to the greater acceptor capacities of pyridinium vs pyridyl groups. The parameter $\Delta\lambda_n^+ = (\lambda_{max})_{cation} - (\lambda_{max})_{neutral}$ is defined as the difference between the intramolecular charge transfer band value of 4DA and 4DA+. The value of this parameter is -75 nm, the established correlation between donor/acceptor strength and $\Delta\lambda_n^+$ suggests that in the present chromophores, intramolecular charge transfer increases with increasing donor/acceptor strength. Since in this case the donor and acceptor units are identical, the increased polarizabilities of 4DA+ is the result of an increased number of delocalized π electrons, hence extension of the effective conjugation length.

5.1 Absorption and Emission Spectra

The measurements of absorption and fluorescence spectra where performed on diluted solutions ($c = 5 * 10^{-6}$ M or less) in ethanol, and are showed in Figure 5.2 The absorption spectrum shows an intense intramolecular charge transfer (CT) band whit the maximum at 515 nm. The asymmetric shape is well fitted with two Gaussian curves centered to 526 and 495 nm. In addition a weak shoulder can be observed around 380 nm. The molar extinction coefficient ε at the maximum is evaluated to be a 142 800 mol^{-1} L cm^{-1} corresponding a very strong transition.

A pattern of excited states is computed for the molecule. The two almost degenerate sets of HOMO→ LUMO excitations give rise to two transitions at the same wavelength of 566 nm (very weak), two transitions at 512 nm and 479 nm (not allowed). The absorption spectrum is therefore dominated by the single very intense transition at 512 nm, constituted by a combination (0.44 and 0.25, respectively) of HOMO-1→LUMO+1– HOMO→LUMO orbital excitations (see Figure orbitali)

The emission spectrum shows a broad band whose maximum is at 590 nm and the fluorescence quantum yield resulted to be a 0.015 using ethanol as a solvent, in solution of DMSO Φ_F is 0.036.[55] The adiabatic energy calculated for this transition is 2.00 eV corresponding to a wavelength of 600 nm, in perfect agreement with the experimental observation.

The Stokes shift, calculated as the difference between the maximum of

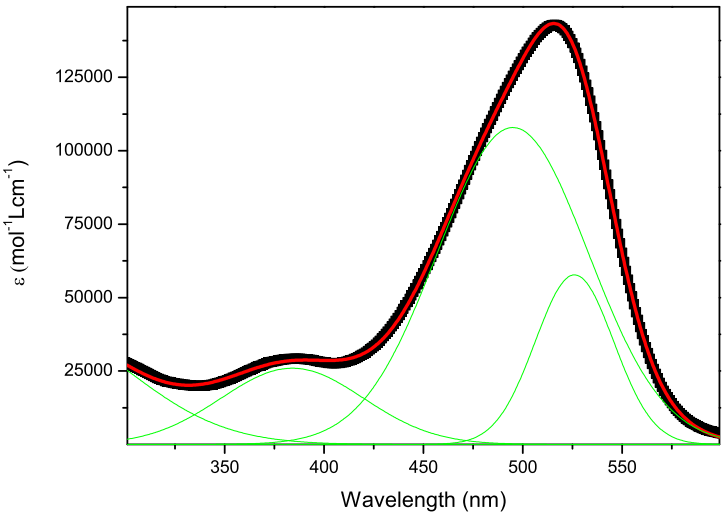

Figure 5.2: UV-Visible spectra (*blackline*) solvent EtOH plotted together with a Gaussian fit (*red*) and individual Gaussians are shows in *green*.

the absorption and the maximum of the emission, in ethanol solution has a value of 2470 cm^{-1}, whereas in DMSO solution this value increases slightly to 4730 cm^{-1}.

5.2 Transient Absorption Spectroscopy

Ultrafast time-resolved transient absorption data were collected in an effort to study the excited-state absorption properties 4DA+ to facilitate kinetic comparisons with the neutral 4DA measurements. The measurements were registered at room temperature using ethanol as solvent. The preparation of the solutions was performed using the technique described above as 'freeze-pump-thaw'. The compound 4DA+ is particularly sensitive to light, at the presence of oxygen in solution, or chlorinated solvents, this has prevented the realization of the experiment in various solvents, as has been done for the neutral compound. In the Figure 5.4 report the transient absorption spectra of the 4DA+ in ethanol in the spectral range 500–680 nm recorded at various delay time after the excitation at 480 nm in resonance with the CT transition. We observed an intense negative band around 590 nm corresponding to the stimulated emission, and a positive band around 525 nm corresponding

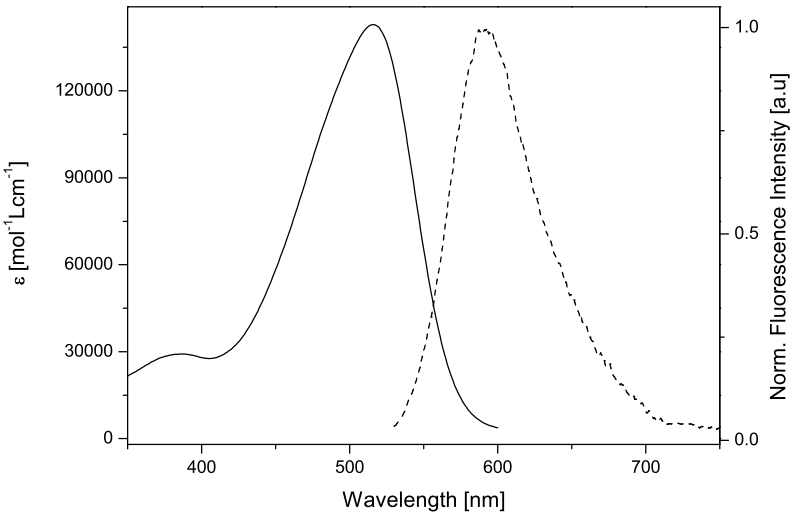

Figure 5.3: UV-Visible absorption (*solid line*) and fluorescence(*dashed line*) spectra of $5*10^{-4}$M solution in ethanol.

to the excited state absorption, partially overlapping at shorter wavelengths with the bleaching signal (not visible in the figure). In the first 10 ps after the excitation an increase of the intensity is observed in the ESA and SE bands . After first 10 ps the signal decay following a single exponential law.

In Figure 5.5 the decays of the signals extracted at significant wavelengths are reported. The fitting required the convolution of the Gaussian shape instrumental function (FWHM = 200 fs) with a multiexponential decay step function. The results are summarized in Table

5.2.1 Singular Value Decomposition

We performed single value decomposition (SVD) to the 4DA+ ligand spectra, in order to estimate the number of spectrally independent components, eliminate random noise, and to store spectral information in a compressed form. The kinetics vectors of the SVD output were fitted by sums of exponentials, yielding phenomenological rates and amplitudes. The decomposition procedure gave two main components characterized by singular values $S_{11} = 6.7$ and $S_{22} = 1.1$. The normalized basis spectra (first two columns of matrix U) are shown in the Figure 5.6.

The evolution of V_1 and V_2 was simulated by the convolution of instru-

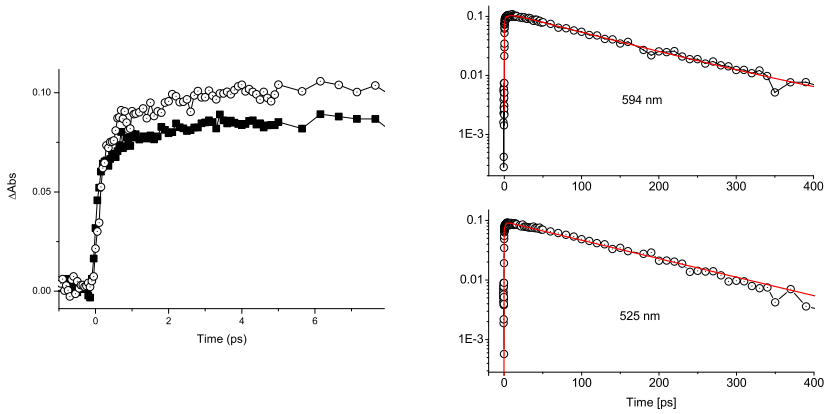

Figure 5.4: Kinetics profiles recorded at the maximum of the ESA band at 525 nm (*full squares*) and at the maximum of the SE band 594 nm (*open circles*) The signal of the differential absorbance of SE signal has been changed to make the comparison between the ESA and SE signals easier. In the right panel shown the transient absorbance at the probe wavelengths for long delay times.

mental function with a three exponential kinetic model. The parameters of the deconvolution/fitting process was showed in the Table 5.1.

	1.58±0.1 (ps)	18 ±0.4(ps)	133 ±10(ps)
SV_1	0.0040	0.13565	0.13418
SV_2	0.309	-0.04725	-0.01418

Table 5.1: Parameters for a simultaneous fit of time courses of single value decomposition components with a three exponential model.

By a first observation of Figure 5.7 we observe that two of the DADS are similar and the third one closing resembles the profile of a spectrum taken at long delay times. We ascribe the first and the second DADS to two different processes. One is the formation of the first excited state leading to the CT state. The broad and weak feature is due to a delocalized state rapidly converting into a state with a large charge transfer character from D to A (see also Figure orbitali for the charge distribution). The second shows clearly a negative band corresponding to the unrelaxed SE. The SVD analysis gives an indication that some process occurs in the first 60 ps that mainly affect SE. Therefore the SE band deserves an additional analysis.

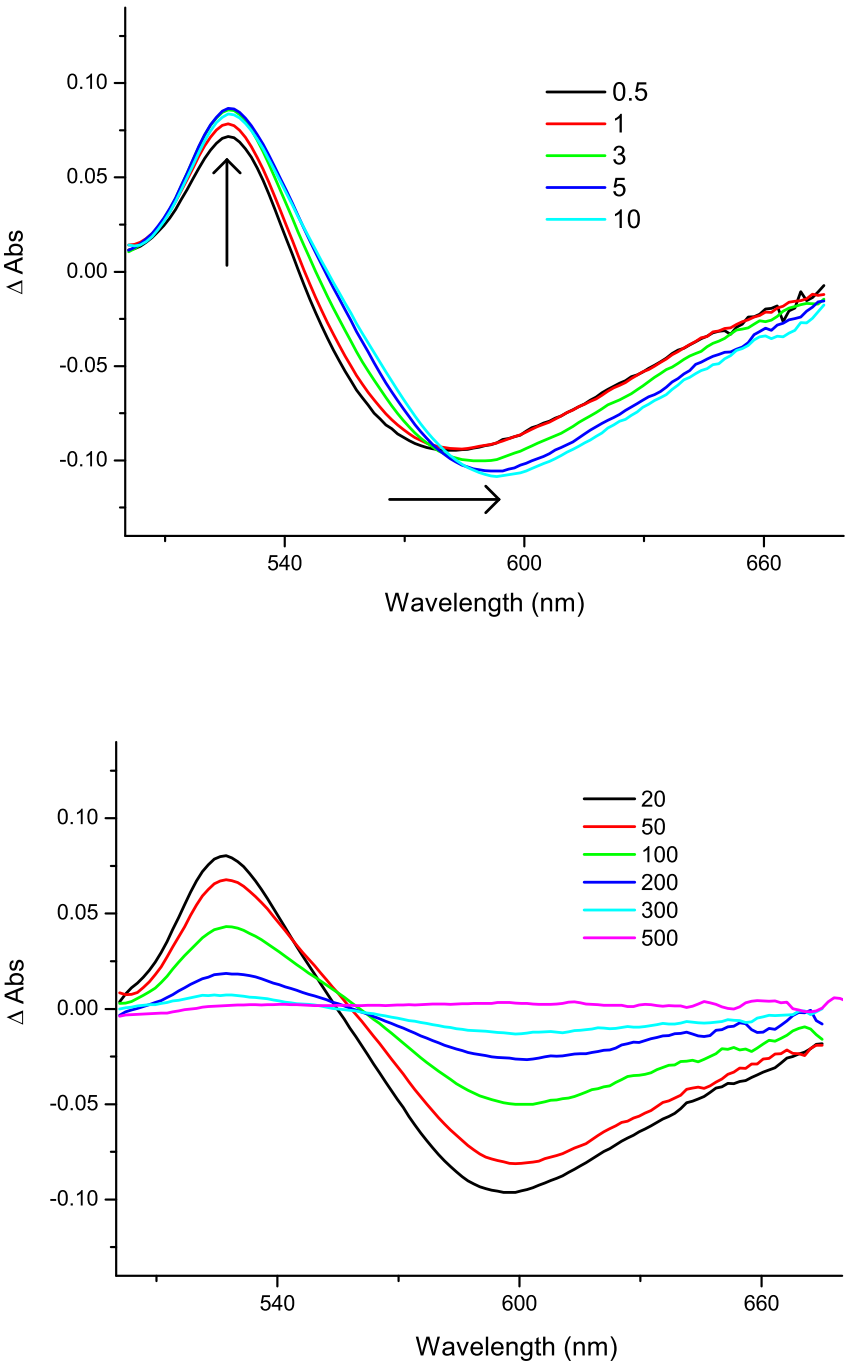

Figure 5.5: Transient absorption spectra of 4DA+ excited at 480 nm with femtosecond pulses (0.4 μJ/pulse). The absorbance of the sample is 0.8 at the pump wavelength. The delay times between pump and probe pulses are reported in the legend, the values are expressed in picoseconds.

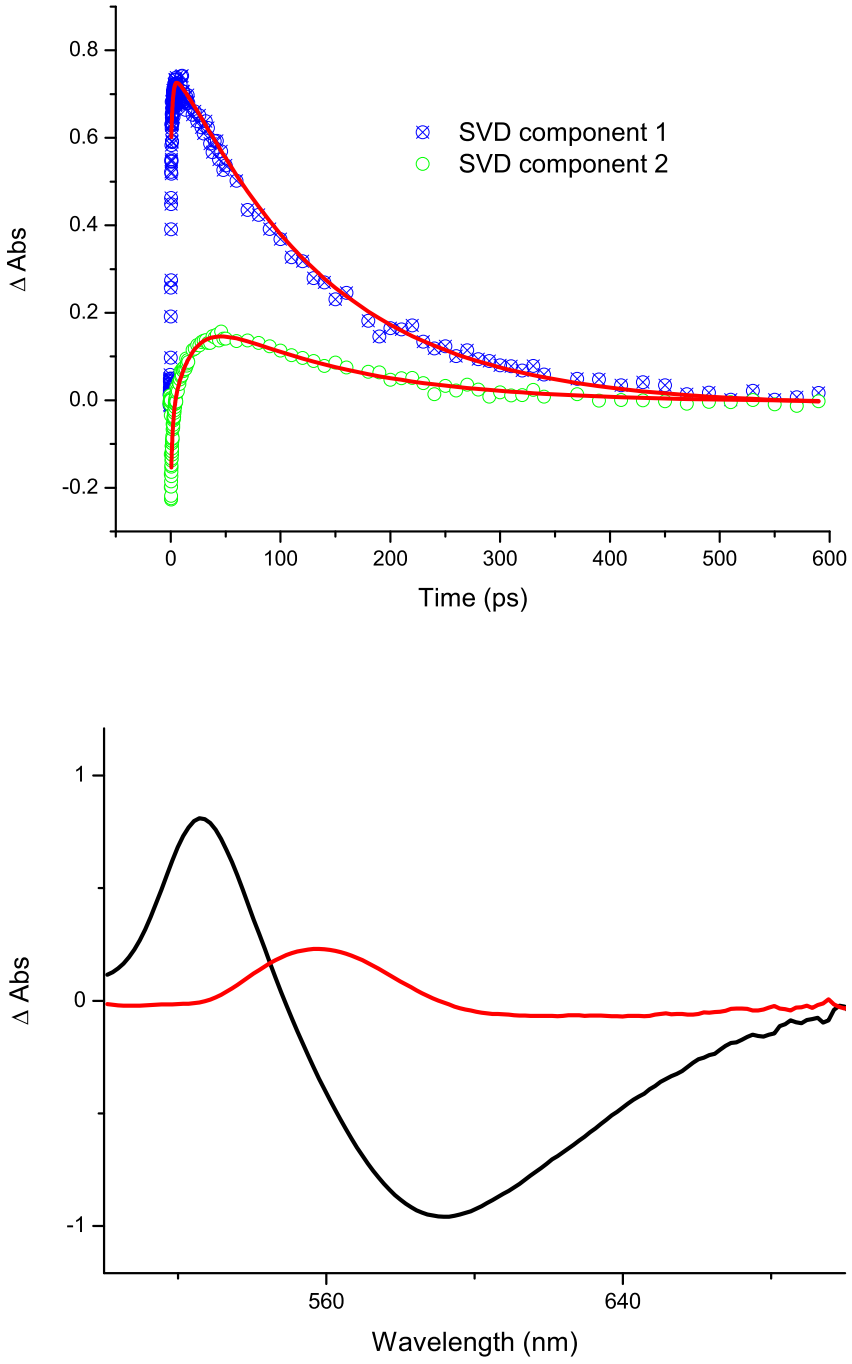

Figure 5.6: Time courses of SVD components of 4DA+ data. The ΔA values are scaled according to the singular value S_{11}=6.7 S_{22}=1.1 . Basis spectra U_1 (*black*) and U_2 (*red*).

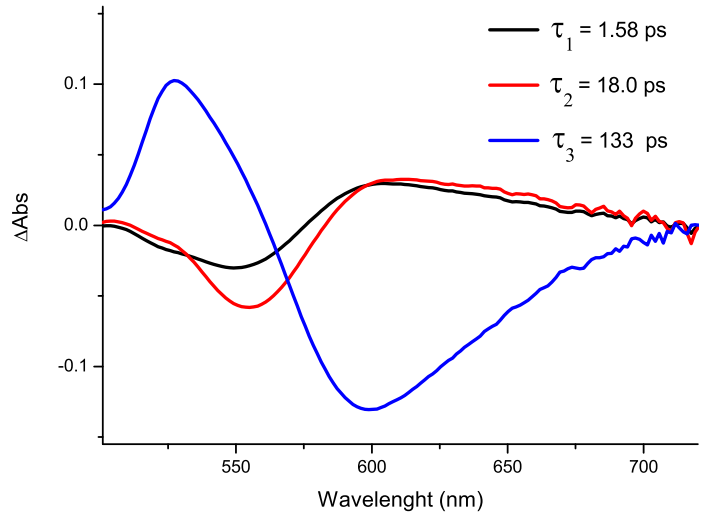

Figure 5.7: Spectral components of the three time contributions to the transient absorption signal in ethanol. $DADS_1$ in black, $DADS_2$ in red and $DADS_3$ in blue.

5.2.2 Dynamic Stokes Shift

If we look at TAS spectra Fig 5.4 , we can see that a shift of the maximum of the SE band occurs in the first picoseconds. Whether this latter is due to an intramolecular dynamics or is due to solvent rearrangement can be understood after the construction of the corresponding correlation function and its comparison to previous data. The dynamics Stokes shift function has been calculated by the Equation 4.6. As a matter of fact, on the contrary of fluorescence spectra obtained by up conversion or directly registered by streak cameras, the shape of SE is distorted, being a stimulated effect and being altered by the possible presence of ESA bands. Both these effects can modify the shape of the band and change its maximum position.[62] However, in the present case the SE and ESA bands are reasonably well separated and it is possible to fit the complete spectrum from 450 to 700 nm, including the ESA band whose position results reproducible at all the delays. This allows to recover the best values for the SE maxima. In addition we observe that if the SE spectra recorded 100 picoseconds after the excitation are compared to the static emission spectra, a good coincidence of the maxima can be observed.

The result of the SE shift analysis provided the correlation curve reported in Figure 5.8. The fitting of the decay is well reproduced by a biexponential curve with τ_1=1.7±0.5 ps (43%) and τ_2=21±0.5 1 ps (57%). Considering the

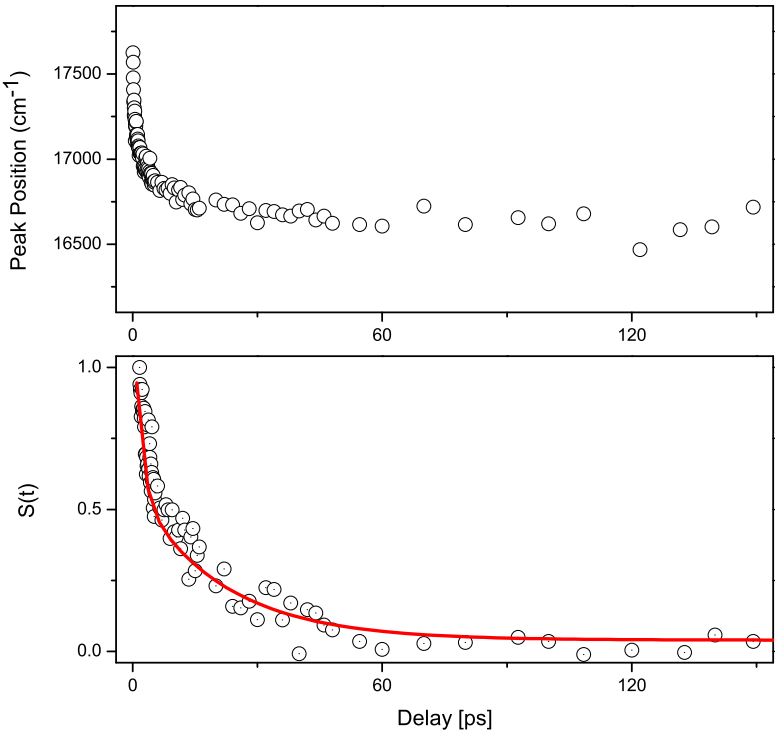

Figure 5.8: (*Upper panel*) Peak position of the SE band against time delay. (*Bottom*) The kinetic traces of the dynamical Stokes shift (*open circles*) using as solvent ethanol. The results of the fitting analysis whit a bi-exponential function (τ_1=1.7±0.5 ps and τ_2=21±0.5 1 ps) is shown in red solid line.

uncertainty introduced by the band maxima analysis we can assert that the time constants obtained in the present study coincide with those reported in a previous study on the dynamical Stokes shift of a dye solution in ethanol (30 fs (8.5%), 390 fs (23%), 5 ps (18.5%), 29,6 ps (50%)).[63] Our data are even more consistent with the previous ones if the average time constants $<\tau>$ are compared (present $<\tau>$= 13 ps, $<\tau>$ = 16 ps).[63]

The good coincidence of the present analysis with those previously reported allows us to state that the origin of the large Stokes shift is entirely due to solvent rearrangement and to rule out any contribution of intramolecular conformational dynamics. This is confirmed by our ab-initio calculations . In fact the *transoid* form was calculated to be more stable by 10.0 kcal mol^{-1} over the *cisoid* one, likely due to the stronger electrostatic repulsion between the two charged arms of the ligand. Thus, the transition

to the excited state involves only minor changes in the structure as can be seen from optimized geometrical parameters for S_0 and S_1 reported in Tab.geometria.

5.3 Conclusions

6

Donor-Acceptor System [6AB]

6.1 Absorption and Emission Spectra

6.2 Transient Absorption Spectroscopy

6.2.1 Measurements in

6.2.2 Singular Value Decomposition

6.3 Steady State FTIR Spectra

6.4 Time-Resolved Infrared Spectroscopy

6.4.1 Measurements in Chloroform

6.4.2 Measurements in CCl4

6.5 Conclusions

7

Bibliography

[1] Foster, R. *Organic Charge Transfer Complexes;* Academic Press Inc., 1969.

[2] Verhoeven, J.; Dirkx, I.; de Boer, T. J. *Tetrahedron* **1969**, *25*, 4037.

[3] Pasman, P.; Mes, G.F.and Koper, N. V. J. *J. Am. Chem. Soc* **1985**, *107*, 5839.

[4] Closs, G.L.; Miller, J. *Science* **1988**, *240*, 440.

[5] Cederbaum, L. S.; Domcke, W.; Köppel, H.; Niessen, W. V. *Chemical Physics* **1977**, *26*(2), 169 – 177.

[6] Mahapatra, S.; Worth, G. A.; Meyer, H.-D.; Cederbaum, L. S.; Kappel, H. *The Journal of Physical Chemistry A* **2001**, *105*(23), 5567–5576.

[7] Clifford, S.; Bearpark, M. J.; Bernardi, F.; Olivucci, M.; Robb, M. A.; Smith, B. R. *Journal of the American Chemical Society* **1996**, *118*(31), 7353–7360.

[8] A. B. Trofimov, H. K.; Schirmer, J. **1998**, *109*, 1025.

[9] Clemens Woywod, Wolfgang Domcke, A. L. S.; Werner, H. J. *J. Chem. Phys.* **1994**, *100,*, 1400.

[10] A. Raab, G. A. Worth, H.-D. M.; Cederbaum, L. S. *J. Chem. Phys.* **1999**, *110*, 936.

[11] Kohler, B. E. *Chemical Reviews* **1993**, *93*(1), 41–54.

[12] Fernando Bernardi, M. O.; Robb, M. A. *Chem. Soc. Rev.„ 25, 321-328* **1996**, *25*, 321.

[13] Bearpark, M. J.; Bernardi, F.; Clifford, S.; Olivucci, M.; Robb, M. A.; Smith, B. R.; Vreven, T. *Journal of the American Chemical Society* **1996**, *118*(1), 169–175.

[14] Olivucci, M.; Ragazos, I. N.; Bernardi, F.; Robb, M. A. *Journal of the American Chemical Society* **1993**, *115*(9), 3710–3721.

[15] Garavelli, M.; Celani, P.; Bernardi, F.; Robb, M. A.; Olivucci, M. *Journal of the American Chemical Society* **1997**, *119*(29), 6891–6901.

[16] Sanchez-Galvez, A.; Hunt, P.; Robb, M. A.; Olivucci, M.; Vreven, T.; Schlegel, H. B. *Journal of the American Chemical Society* **2000**, *122*(12), 2911–2924.

[17] Boggio-Pasqua, M.; Bearpark, M. J.; Hunt, P. A.; Robb, M. A. *Journal of the American Chemical Society* **2002**, *124*(7), 1456–1470.

[18] W. FuSS, W. E. S.; Trushin, S. A. *J. Chem. Phys. ,* **2000**, *112*, 8347.

[19] Trushin, S. A.; Fuß, W.; Schmid, W. E. *Chemical Physics* **2000**, *259*(2-3), 313 – 330.

[20] Angulo, G.; Grilj, J.; Vauthey, E.; Serrano-Andres, L.; Rubio-Pons, O.; Jacques, P. *Chem. Eur. J. of Chem. Phys.* **2010**, *11*(2), 480–488.

[21] Stolow, A. *International Reviews in Physical Chemistry* **2003**, *22*(2), 377–405.

[22] Domcke, W.; Stock, G. *Theory of Ultrafast Nonadiabatic Excited-State Processes and their Spectroscopic Detection in Real Time;* John Wiley & Sons, Inc., 2007.

[23] Worth, G. A.; Cederbaum, L. S. *Annu. Rev. Phys. Chem.* **2004**, *55*, 127–58.

[24] Hahn, S.; Stock, G. *The Journal of Physical Chemistry A* **2001**, *105*(12), 2626–2633.

[25] Stuart Althorpe, G. W., Ed. *Quantum Dynamics at Conical Intersections;* 2004.

[26] Manthe, U.; Koppel, H. *J. Chem. Phys.* **1990**, *93*, 1658.

[27] Pancur, T.; Renth, F.; Temps, F.; Harbaum, B.; Krager, A.; .Herges, R. *Phys Chem Chem Phys 7(9):1985-9 (2005)* **2005**, *7*, 1985.

[28] P. Foggi, L. B.; Neuwahl, F. V. R. *International Journal of Photoenergy* **2001**, *3*, 103–109.

[29] Berera, R.; van Grondelle, R.; Kennis, J. T. M. *Photosynth Res* **2009**, *101*, 105–118.

[30] Danielius, R.; Piskarskas, A.; Trapani, P. D.; Andreoni, A.; Solcia, C.; Foggi, P. Sep **1996**, *35*(27), 5336–5339.

[31] M. Ziolek, M. Lorenc, R. N. *Applied Physics B* **2001**, *71*, 843–847.

[32] m. lorenc1 M. Ziolek, R. Naskrecki, J. K. J. J. A. M. *Applied Physics B* **2002**, *74*, 19–27.

[33] Rini, M.; Dreyer, J.; Nibbering, E.; Elsaesser, T. *Chemical Physics Letters* **2003**, *374*, 13.

[34] Brunner, W.; Paul, H. In Wolf, E., Ed., *Progress in Optics XV*, Vol. XV. North-Holland, 1977.

[35] Dmitriev, V.; Gurzadyan, G.; Nikogosyan, D. *Handbook of Nonlinear Optical Crystals*, Vol. 64 of *Springer Series in Optical Science;* Springer, third ed., 1999.

[36] Petrov, V.; Rotermund, F.; Noack, F. *Journal of Optics A: Pure and Applied Optics* **2001**, *3*(3), R1.

[37] Hamm, P.; Kaindl, R. A.; Stenger, J. *Opt. Lett.* **2000**, *25*, 1798–1800.

[38] Rotermund, F.; Petrov, V.; Noack, F. *Optics Communications* **2000**, *185*(1-3), 177–183.

[39] Kaindl, R. A.; Wurm, M.; Reimann, K.; Hamm, P.; Weiner, A. M.; Woerner, M. Dec **2000**, *17*(12), 2086–2094.

[40] Seilmeier, A.; Worner, M.; Hubner, H.-J.; Kaiser, W. *Applied Physics Letters* **1988**, *53*(25), 2468–2470.

[41] Sutherland, R. L. *Handbook of Nonlinear Optics;* Marcel Dekker Inc, 1996.

[42] Shen, Y. R. *The Principles of Nonlinear Optics;* Wiley: New York, 1984.

[43] Alfano, R. *The Supercontinuum Laser Source;* Springer-Verlag Berlin and Heidelberg GmbH & Co. K, 1989.

[44] Agrawal, G. P.; Baldeck, P. L.; Alfano, R. R. Nov **1989**, *40*(9), 5063–5072.

[45] Hsieh, H.-T.; Psaltis, D.; Beyer, O.; Maxein, D.; Buse, K.; Sturman, B. *Journal of Applied Physics* **2005**, *97*(11), 113107.

[46] Whitten, D. G.; Lee, Y. J. *Journal of the American Chemical Society* **1972**, *94*(26), 9142–9148.

[47] Vencel, T.; J. Donovalona, J.and Gaplovsky, A.; T. Kimura, T.; Š. Toma. *Chem. Pap.* **2005**, *59*, 271–274.

[48] Lakowicz, R. *Principles of Fluorescence Spectroscopy;* Kluwer, New York, 2nd ed.„ (1999).

[49] Lewis, J.; Maroncelli, M. *Chemical Physics Letters* **1998**, *282*(2), 197 – 203.

[50] Kaes, C.; Katz, A.; Hosseini, M. W. *Chemical Reviews* **2000**, *100*(10), 3553–3590.

[51] Castellucci, E.; Angeloni, L.; Marconi, G.; Venuti, E.; Baraldi, I. *The Journal of Physical Chemistry* **1990**, *94*, 1740–1745.

[52] Buntinx, G.; Naskrecki, R.; Poizat, O. *The Journal of Physical Chemistry* **1996**, *100*(50), 19380–19388.

[53] Buntinx, G.; Poizat, O.and Valat, P.; Wintgens, V.; Righini, R.; Foggi, P. *J. Chim. Phys.* **1993**, *90*, 1733–1748.

[54] Mazzucato;, S.; Fortunati;, I.; Scolaro;, S.; Zerbetto;, M.; Ferrante;, C.; Signorini;, R.; Pedron;, D.; Bozio;, R.; Locatelli;, D.; Righetto;, S.; D.Roberto.; Ugo;, R.; Abbotto;, A.; Archetti;, G.; Beverina, L.; Ghezzi, S. *Physical Chemistry Chemical Physics* **2007**, *9*, 2999–2005.

[55] Abbotto, A.; Bellotto, L.; De Angelis, F.; Manfredi, N.; Marinzi, C. *Eur. J. Org. Chem.* **2008**, (30), 5047–5054.

[56] Bradamante, S.; Facchetti, A.; Pagani, G. A. *J. Phys. Org. Chem.* **1997**, *10*(7), 514–524.

[57] Gaussian 03, Revision C.02. Frisch, M. J.; Trucks, G. W.; Schlegel, H. B.; Scuseria, G. E.; Robb, M. A.; Cheeseman, J. R.; Montgomery, Jr., J. A.; Vreven, T.; Kudin, K. N.; Burant, J. C.; Millam, J. M.; Iyengar, S. S.; Tomasi, J.; Barone, V.; Mennucci, B.; Cossi, M.; Scalmani, G.; Rega, N.; Petersson, G. A.; Nakatsuji, H.; Hada, M.; Ehara, M.; Toyota, K.; Fukuda, R.; Hasegawa, J.; Ishida, M.; Nakajima, T.; Honda, Y.; Kitao, O.; Nakai, H.; Klene, M.; Li, X.; Knox, J. E.; Hratchian, H. P.; Cross, J. B.; Bakken, V.; Adamo, C.; Jaramillo, J.; Gomperts, R.; Stratmann, R. E.; Yazyev, O.; Austin, A. J.; Cammi, R.; Pomelli, C.; Ochterski, J. W.; Ayala, P. Y.; Morokuma, K.; Voth,

G. A.; Salvador, P.; Dannenberg, J. J.; Zakrzewski, V. G.; Dapprich, S.; Daniels, A. D.; Strain, M. C.; Farkas, O.; Malick, D. K.; Rabuck, A. D.; Raghavachari, K.; Foresman, J. B.; Ortiz, J. V.; Cui, Q.; Baboul, A. G.; Clifford, S.; Cioslowski, J.; Stefanov, B. B.; Liu, G.; Liashenko, A.; Piskorz, P.; Komaromi, I.; Martin, R. L.; Fox, D. J.; Keith, T.; Al-Laham, M. A.; Peng, C. Y.; Nanayakkara, A.; Challacombe, M.; Gill, P. M. W.; Johnson, B.; Chen, W.; Wong, M. W.; Gonzalez, C.; Pople, J. A.

[58] Glik, E. A.; Kinayyigit, S.; Ronayne, K. L.; Towrie, M.; Sazanovich, I. V.; Weinstein, J. A.; Castellano, F. N. *Inorganic Chemistry* **2008**, *47*(15), 6974–6983.

[59] Elsaesser, T.; Kaiser, W. *Annual review of physical chemistry* **1991**, *42*, 83–87.

[60] Facchetti, A.; Beverina, L.; van der Boom, M. E.; Dutta, P.; Evmenenko, G.; Shukla, A. D.; Stern, C. E.; Pagani, G. A.; Marks, T. J. *Journal of the American Chemical Society* **2006**, *128*(6), 2142–2153.

[61] Lorenc, M.; Ziolek, M.; Naskrecki, R.; Karolczak, J.; Kubicki, J.; Maciejewski, A. *Applied Physics B: Lasers and Optics* **2002**, *74*, 19–27.

[62] Joo, T.; Jia, Y.; Yu, J.-Y.; Lang, M. J.; Fleming, G. R. *The Journal of Chemical Physics* **1996**, *104*(16), 6089–6108.

[63] Bagchi, B.; Jana, B. *Chemical Society Reviews* **2010**, *39*, 1936–1954.

[64] Spry, D. B.; Goun, A.; Fayer, M. D. *The Journal of Physical Chemistry A* **2007**, *111*(2), 230–237.

[65] Becker, H.-C.; Kilså, K. *Spectrochimica Acta Part A: Molecular and Biomolecular Spectroscopy* **2009**, *72*(5), 1014 – 1019.

[66] Rice, J. K.; Baronavski, A. P. *The Journal of Physical Chemistry* **1992**, *96*(8), 3359–3366.

[67] Abraham, E.; Oberlè, J.; Jonusauskas, G.; Lapouyade, R.; Rullière, C. *Journal of Photochemistry and Photobiology A: Chemistry* **1997**, *105*(2-3), 101 – 107.

[68] Zachariasse, K.; Grobys, M.; von der Haar, T.; Hebecker, A.; Il'ichev, Y.; Jiang, Y.-B.; Morawski, O.; Kühnle, W. December **1996**, *102*(1, Supplement 1), 59–70.

[69] Hamm, P. *Chemical Physics* **1995**, *200*(3), 415 – 429.